Earth and Planetary Science Letters 490 (2018) 206–215

Contents lists available at ScienceDirect

Earth and Planetary Science Letters

www.elsevier.com/locate/epsl

Impact-melt hygrometer for Mars: The case of shergottite Elephant Moraine (EETA) 79001

Yang Liu [a,*], Yang Chen [a], Yunbin Guan [b], Chi Ma [b], George R. Rossman [b], John M. Eiler [b], Youxue Zhang [c]

[a] Jet Propulsion Laboratory, California Institute of Technology, Pasadena, CA 91109, USA
[b] Division of Geological and Planetary Sciences, California Institute of Technology, Pasadena, CA 91125, USA
[c] Department of Earth and Environmental Sciences, University of Michigan, Ann Arbor, MI 48109, USA

ARTICLE INFO

Article history:
Received 14 November 2017
Received in revised form 8 March 2018
Accepted 12 March 2018
Available online xxxx
Editor: F. Moynier

Keywords:
Martian volatiles
impact melts
subsurface water
magmatic water
Mars

ABSTRACT

We report volatile concentrations and hydrogen isotope compositions of impact melts and minerals in EETA 79001. We observed chemical changes in pyroxene, maskelynite (or feldspathic glass), and merrillite in contact with or inside impact melts. All pyroxene grains analyzed here are inside or close to impact melt pockets and contain 10–41 ppm H_2O and enriched in D ($\delta D = +1729$ to $+3707‰$), with the highest values found in a grain enclosed in an impact melt pocket. Maskelynite or feldspathic glass contains 6.3 to 98 ppm H_2O with δD values of $+1604$ to $+3938‰$. The high H_2O and δD values were obtained in those enclosed inside or in contact with the impact melts, whereas low H_2O content (4 ppm) and terrestrial-like D/H value (δD of $-90 \pm 82‰$) were found in one maskelynite grain away from impact melts contains. Rims of ~5 μm thickness of merrillite grains next to impact melts display Na-depletion by ~0.9 wt%, and the sides in contact with impact melts show Mg-enrichment by ~0.5 wt%. However, the H_2O and δD values of merrillite interiors (39–242 ppm H_2O and δD of $+1682$ to $+3884‰$) do not show correlation with their proximity to the impact melts. Rather, δD and $1/H_2O$ of merrillite form a negative trend different from that of impact melt pockets and maskelynite, suggesting post-crystallization or late-crystallization interactions with the crustal fluids.

The impact melt pockets in EETA 79001 contain 121–646 ppm H_2O, 4.3–13 ppm F, 13–50 ppm Cl, 707–2702 ppm S, and the δD values of $+3368$ to $+4639‰$. The correlations between H_2O, F, Cl, P_2O_5, and δD values of impact melts and feldspathic glass are consistent with mixing between a volatile-rich and high δD ($+3000$ to $+5000‰$) endmember and a volatile-poor and low δD endmember. The volatile-poor and low δD endmember is consistent with magmatic volatiles stored in silicates. The volatile-rich and high δD endmember represents pre-impact alteration materials by subsurface water. Alteration from the subsurface water, equilibrated with the present-day-like Martian atmosphere, occurred after the crystallization of the rock (~170 Ma) and before impact launch (~0.7 Ma). Our conclusion is different from the previous suggestion of an isotopically distinct subsurface water reservoir with a δD value of $+1000$ to $+2000‰$ in EETA 79001. Although heterogeneous subsurface water on Mars is possible, the previous study was likely biased by a limited number of analyses ($n = 2$) and possible terrestrial contamination. The δD value of the subsurface source in EETA 79001 is ~$+4200‰$, similar to those in the Tissint meteorite (crystallization at ~600 Ma, impact launch at ~0.7 Ma) and LAR 06319 (crystallization at ~200 Ma, impact launch at ~3 Ma), suggesting stable water chemistry for the subsurface environment in the last 600 Myrs.

1. Introduction

Hydrogen isotope compositions of the Martian surface and subsurface water are direct witnesses to the atmosphere and climate evolution on Mars (e.g., Owen et al., 1988; Jakosky, 1991; Villanueva et al., 2015). Highly elevated D/H values ($\sim 9 \times 10^{-4}$) of trace amounts of moisture in the present-day Martian atmosphere attest significant water loss from a water-rich past (Webster et al., 2013), which is consistent with mineralogical and morphological observations (e.g., Bibring et al., 2006; Carr and Head, 2010). Although the spatial distribution of D/H values of the modern Mar-

* Corresponding author.
E-mail address: Yang.Liu@jpl.nasa.gov (Y. Liu).

https://doi.org/10.1016/j.epsl.2018.03.019
0012-821X/

tian atmosphere can elucidate current Martian surface water reservoirs (e.g., Villanueva et al., 2015), these values are still a single point in time. To understand the evolution history of the Martian atmosphere and climate, hydrogen isotope analysis of surface water or the relevant products at different ages and locations is needed. Such data are sparse. Besides present-day atmosphere, the only direct measurement of D/H value of surface water is from clay minerals in the ~3.0 Ga sedimentary rocks at Gale crater (Mahaffy et al., 2015). Indirect information was obtained for crustal water from D/H values of apatite (Greenwood et al., 2008). However, although Boctor et al. (2003) showed (sub)surface water signatures in impact melts in shergottites, the unique capability of impact melt pockets providing subsurface water from different times and locations has been largely overlooked until recently.

Impact melt pockets are spherical to elliptical regions containing shock-induced melt (now glass) that are common in shergottites (e.g., Walton and Shaw, 2009). Large impact melt pockets with diameters from 100 μm to ~1 cm most likely formed at the expense of pre-existing vesicles. The large contrast in shock impedance between rock and air can lead to sufficient energy to melt materials in the vesicles and minerals around them (Wiens, 1988; Wiens and Pepin, 1988; Bogard et al., 1989; Beck et al., 2007). Mantle sources for shergottites contain ~14–73 ppm H_2O (McCubbin et al., 2016). Thus, vesicles are expected in pre-shock basalts, since volatile saturation can be reached during melting, ascent, and subsequent fractionation of the partial melt from mantle. These vesicle-bearing basalts would have resided in the near-surface environment for 100s Myrs before their impact launch. In this long residence time, these igneous rocks have plenty of chances to react with crustal fluids (Gooding et al., 1991; Treiman et al., 1993; Hu et al., 2014). Presence of crustal fluids is a reasonable assumption based on the detection of subsurface water (e.g., Boynton et al., 2002). Because vesicles present a pathway for fluids, they are ideal locations to host alteration materials. When shergottites were launched from Mars by discrete impacts, shock generated by the impact collapsed nearly all void spaces, rendering a vesicle-free appearance, although residue vesicles can be found as large irregular voids in melt pockets (Fig. 1). Shock melted materials in and around the void space, which subsequently quenched under elevated pressure to impact melt pockets (e.g., Beck et al., 2007; Walton and Shaw, 2009). Similarly, pre-shock alteration along fractures may have been assimilated into shock melt veins. Therefore, impact melt pockets in shergottites are a unique hygrometer for examining not only the subsurface water chemistry, but also the magmatic volatiles of the pre-impact rocks (OH stored in the nominally anhydrous minerals, NAMs). Chen et al. (2015a) demonstrated that different volatile sources in Tissint impact melts can be distinguished by correlated analyses of D/H ratios, volatile abundances, and elemental chemistry.

Despite being common features in shergottites (e.g., Walton and Shaw, 2009), only melt pockets in three shergottites, Tissint, EETA 79001, and LAR 06319, have been analyzed for correlated H isotopes, H, F, Cl, CO_2, and elemental analyses (Chen et al., 2015a, 2015b; Usui et al., 2015; Mane et al., 2016; Kuchka et al., 2017). Even within the limited data, there is discrepancy between subsurface water reservoir inferred from impact melts of EETA 79001. Boctor et al. (2003) reported δD values of +1697 to +2900‰ in the impact melts in EETA 79001, which indicate δD of the subsurface source is higher than +2900‰. Usui et al. (2015) obtained two analyses of a small impact melt (~20 μm by ~70 μm) in EETA 79001 maskelynite and proposed a subsurface water reservoir with δD of +1000 to +2000‰. Parallel to Usui et al. (2015), we investigated large impact melt pockets in EETA 79001 and observed higher δD values than previous studies. Here, we present detailed data of large impact melt pockets (>1 mm), new findings of impact melt effects on OH and D/H compositions of maskelynite and pyroxene in or near impact melts, and chemical effects on merrillite next to impact melt. Our data indicate that the D/H composition of subsurface water in EETA 79001 impact melt pockets is similar to those equilibrated with the Martian atmosphere with a D/H value similar to the present-day. We discuss the potential causes of discrepancy between our inference of subsurface reservoir and that by Usui et al. (2015). In addition, we compare magmatic and subsurface water signatures inferred from impact melts in EETA 79001 with information on Tiissint and LAR 06319.

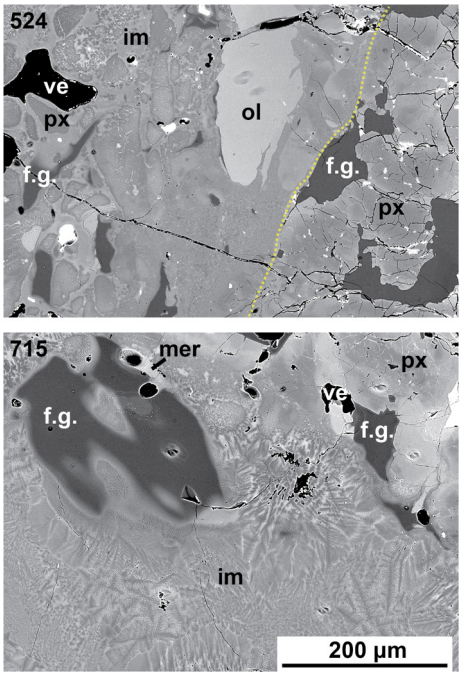

Fig. 1. Back-scattered electron (BSE) images of two impact melt pockets. (Top) An area in a large impact melt pocket in EETA 79001, 524 (Fig. S1), containing rounded olivine and pyroxene that were not yet fully melted and mixed. The dotted curve marks the boundary between the pocket and the rock. (Bottom) An area of a polished chip from EETA 79001, 715 (Fig. S3), taken from a large impact melt pocket. Both impact melts contain irregular shaped pores (Figs. S1–S2). ol – olivine, px – pyroxene, f.g. – feldspathic glass, mer – merrillite, im – impact melt, ve – vesicle.

2. Samples and analytical methods

Large impact melt pockets were found in the olivine-phyric portion (Lithology A) of EETA 79001. The large ones of >1 cm were often referred to as Lithology C, and individual ones were given names (see Mars Sample Compendium, https://curator.jsc.nasa.gov/antmet/mmc/eeta79001.pdf). Three samples from EETA 79001 (524, 715, and 717) were allocated by the Meteorite Working Group at NASA Johnson Space Center. Sample 524 is a polished section of Lithology A mounted in epoxy, containing multiple impact melt pockets and veins (Fig. S1). Sample 715 and 717 are chips from Bravo pocket (~7 mm by 10 mm, Lithology C), which noble gas contents and isotopes was analyzed by Bogard et al. (1984). Two fragments from sample 715 and one chip from sample 717 were polished and mounted in indium (Figs. S2–S4). The original locations of the chips in Bravo pocket are unknown, so the boundaries of impact melt pockets are defined largely based on texture (Figs. S2–S4). Analytical methods are presented in the supplementary materials. In this study, the H_2O contents of all MPI-DING glass standards except for BM90/21-G (Jochum et al., 2006) were determined directly using Fourier Transform InfraRed spectroscopy (FTIR). The H_2O contents of quartz dioritic, basaltic and andesitic

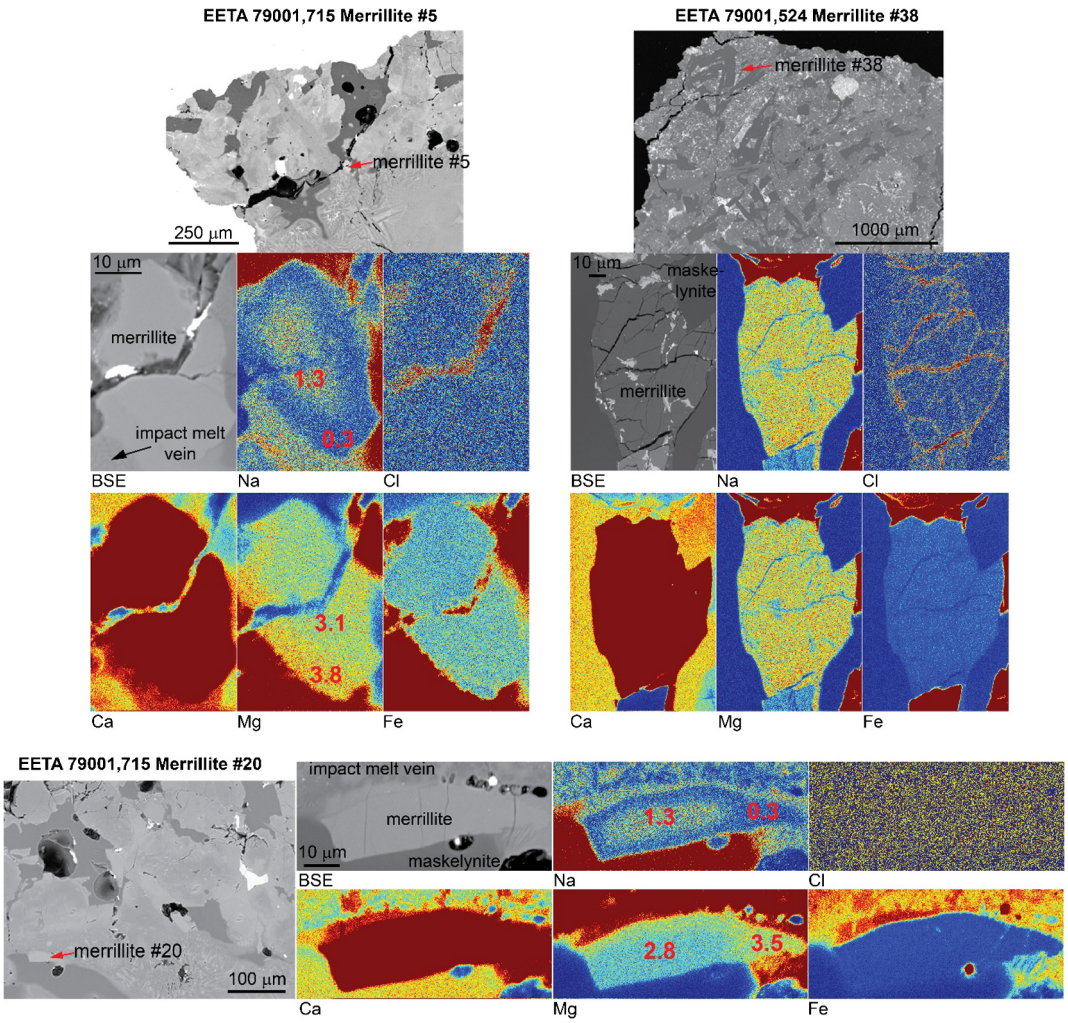

Fig. 2. BSE and X-ray maps of three merrillite grains, showing Na and possible Mg zonation in grains in contact with impact melt (715 merrillite #5, #20), and the lack of zonation in the grain (524 Merrillite #38) about 1 mm away impact melts. Numbers are Na_2O and MgO contents in wt%.

glasses are 34% to 65% of the informative values in Jochum et al. (2006), whereas a rhyolitic glass is ~2.34 times higher (Table S2). We used the FTIR contents for SIMS calibration. The SIMS measurements in Chen et al. (2015a, 2015b) and Kuchka et al. (2017) also used these standards with the FTIR-determined H_2O contents.

3. Results and data interpretation

3.1. Summary of results

The volatile abundances, δD values, and the major element compositions of impact melts and minerals are reported in Tables S3–S6. The impact melt pockets in sample 524 (Lithology A) contain rounded olivine and clinopyroxene, whereas those in sample 715 and 717 (Lithology C) contain glassy regions and dendritic quench crystals (Fig. 1). All samples contain irregular vesicles, glassy regions, and maskelynite or feldspathic glass. The major-element compositions of silicate minerals and merrillite in different samples are indistinguishable from each other (Tables S3–S5). The glassy regions of the impact melts in sample 524 have slightly higher SiO_2, Al_2O_3, CaO, and Na_2O, and lower FeO, MgO, and P_2O_5 than those of impact melts in sample 715 and 717 (Table S5).

A new feature in this study is the Na and Mg zonation of merrillite in contact with impact melts in sample 715, in contrast to those away from impact melts with no zonation (Fig. 2). The circumferential rim (~5 μm thick) contains ~0.3 wt% Na_2O, less than the center of ~1.3 wt% Na_2O. The side at the contact with the impact melts contains higher MgO (~0.7 wt%) than the center of the grains (Fig. 2). The Ca and Fe concentrations are uniform in merrillite grains, regardless of the presence of impact melts.

3.2. Evaluation of terrestrial contamination

The terrestrial contamination in EETA 79001 may include terrestrial weathering of the meteorite, because it is an Antarctica find with a terrestrial residence time of 12 ± 2 kyr (e.g., Jull and Donahue, 1988). Carbonates are typical weathering products in cracks (e.g., Crozaz et al., 2003). Although there are no clear signs of carbonates in samples studied (Figs. 1, 2, S1, and S4), terrestrial contamination could be present in micro-cracks underneath the surface (e.g., Crozaz et al., 2003). An advantage of studying impact melt pockets is that they tend to contain few micro-cracks compared to minerals.

The terrestrial contamination also involves H and C introduced by laboratory sample preparation. Typical preparation methods use water during cutting and polishing of samples. A recent technique is to prepare samples without water in an effort to eliminate terrestrial contamination. However, because SIMS only measures H and C, any material with H and C (polishing paper or cloth) introduces contamination into pits or micro-cracks that are common in Martian meteorites. For example, Usui et al. (2012) showed that only 3 to 4 melt inclusions out of >20 inclusions were

un-contaminated despite that the samples were prepared without water. Mane et al. (2016) carefully compared analyses from samples polished with and without water. Even though micro-cracks-bearing minerals in wet-polished samples are more prone to terrestrial contamination, dry-polished samples still display contamination (Mane et al., 2016). These previous studies emphasized sample preparation is a lesser issue than avoiding micro-cracks during and after the SIMS analysis in minimizing terrestrial contamination. We used similar approaches as in Chen et al. (2015a) to minimize terrestrial contamination. The top surface (~1 μm) that was affected by sample preparation was typically blasted away by the pre-analysis sputtering of the sample, and $^{16}O^{1}H^{-}$ was monitored during the sputtering to ensure complete removal of the affected surface layer. During SIMS analysis, the area to be analyzed was examined using the $^{12}C^{-}$ and $^{16}O^{1}H^{-}$ imaging to avoid micro-cracks or holes. After SIMS analysis, each analytical spot was examined with SEM, and points with cracks or vesicles were excluded from all plots (Table S7 and Fig. S6), although only some of these points show anomalously high $^{12}C^{-}/^{18}O^{-}$ values (Table S7). Moreover, analyses of the epoxy-mounted sample (524) exhibit no difference in H_2O and δD values from those mounted in indium (715 and 717), suggesting that epoxy contributed negligible H background in SIMS analysis. Overall, careful selection of analytical spots leads to better analyses with less terrestrial contamination.

Given the long residence time of EETA 79001 on Earth, diffusive gain of meteoritic water into glass in impact melt pockets or veins needs to be evaluated. If impact glass pockets were exposed, assuming that the meteorite was in Antarctica ice at 0 °C for 12 kyr (Jull and Donahue, 1988), the mean H_2O diffusion distance (or half-fall distance) would be ~2.4 μm using equation (1) in Anovitz et al. (2006). This is a relatively small hydration distance. Moreover, the glass pockets are protected by surrounding minerals. The diffusive gain in minerals is minimum since water is not easily incorporated in mineral structure at surface pressure (Rauch and Keppler, 2002; Kovács et al., 2012). In addition, the low capacity to incorporate H_2O by nominally anhydrous minerals also minimizes diffusive gain of H_2O by melt/glass pockets surrounded by these minerals (Zhang and Liu, 2012). As demonstrated by the data presented below, all impact melts show low H_2O concentrations and high δD values. However, depending on the permeability, impact melts from different regions of the sample may have different degrees of terrestrial water in-gassing. Such effect is difficult to quantify since initial Martian water in different impact melts are likely different. On the basis of the generally large positive δD values of impact melts ($> +3300‰$), we conclude that terrestrial water in-gassing is minor.

3.3. Volatile contents and hydrogen isotope compositions of impact melts and other phases

Most olivine, pyroxene, and maskelynite/feldspathic glass analyzed are in contact with or inside impact melts and veins. Olivine and pyroxene far away from impact melts contain too many micro-cracks, clean analysis without terrestrial contamination could not be obtained in this study. Two olivine grains next to impact melts contain low amounts of H (4 and 7 ppm H_2O) with low δD values (-146 and $-55‰$ in Table S3). Three clinopyroxene grains inside or next to large impact melt pockets contain 10–41 ppm H_2O and δD of $+1729 \pm 259‰$ and $+2837 \pm 245‰$ (Table S3, Fig. S5).

In this study, we define feldspathic glass as those with anhedral shape and maskelynite as those with subhedral shape (Figs. S2 and S5). Nine spots of feldspathic glass ($Ab_{35-47}An_{64-52}$) and three maskelynite grains were analyzed (Fig. 3a). Feldspathic glass in Lithology C melt pockets ($n = 2$, sample 715) contains detectable F (0.64 and 0.49 ppm) and higher δD ($+3797$ and $+3938‰$, Table S4) than feldspathic glass and maskelynite in Lithology A (sample 524) with $\delta D < +2850‰$ ($n = 7$). The maskelynite grain in sample 524 (524-12), away from impact melt, contains very-low H content (~4 ppm H_2O) and a low δD value ($-91 \pm 82‰$). One grain in sample 715 (715-1-24) contains low H content (~6 ppm H_2O) but is enriched in D ($\delta D = +2923 \pm 340‰$). Excluding this point (see below for impact melt effects), the δD and $1/H_2O$ data of the rest of maskelynite data form a linear trend similar to that of impact melts.

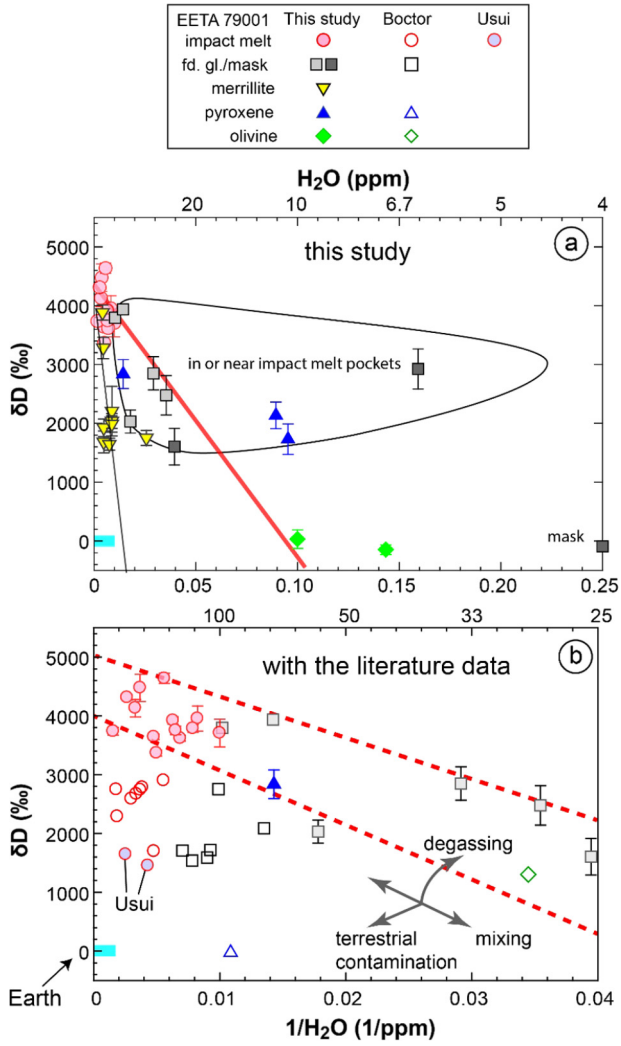

Fig. 3. δD and $1/H_2O$ variation in EETA 79001 impact melts and minerals. (a) Our results. Thick line shows the fit of impact melt data with a y-axis intercept of $+4200 \pm 440‰$ (2σ, $n = 16$). Thin line is the fit of merrillite (excluding one point) with an intercept at $+3900 \pm 2500‰$ (2σ, $n = 6$). Dark squares are maskelynites, lighter squares are feldspathic glass. (b) Comparison with the literature data on EETA 79001. A smaller range of $1/H_2O$ is plotted to better illustrate the differences between the literature data and this study. Data from Boctor et al. (2003) are open symbols, two analyses of an impact melt from Usui et al. (2015) are lightly filled circles. Dashed lines show potential bounds of the subsurface volatile values. (For interpretation of the colors in the figure(s), the reader is referred to the web version of this article.)

Merrillite grains from different locations (near or away from impact melts) contain 39–242 ppm H_2O and δD of $+1645$ to $+3884‰$ (Table S4). Fluorine and sulfur in merrillites are below SIMS backgrounds (1 ppm and 0.1 ppm, respectively). The δD and $1/H_2O$ data of merrillite extend from the region of the impact melts to low $1/H_2O$ and low δD values, forming a trend different from maskelynite and impact melts (Fig. 3a).

Impact melt pockets and veins in different samples contain 121–646 ppm H_2O, 4.3–13 ppm F, 13–50 ppm Cl, and 731–2702 ppm S (Fig. 4a, Table S3). Impact melts and veins in

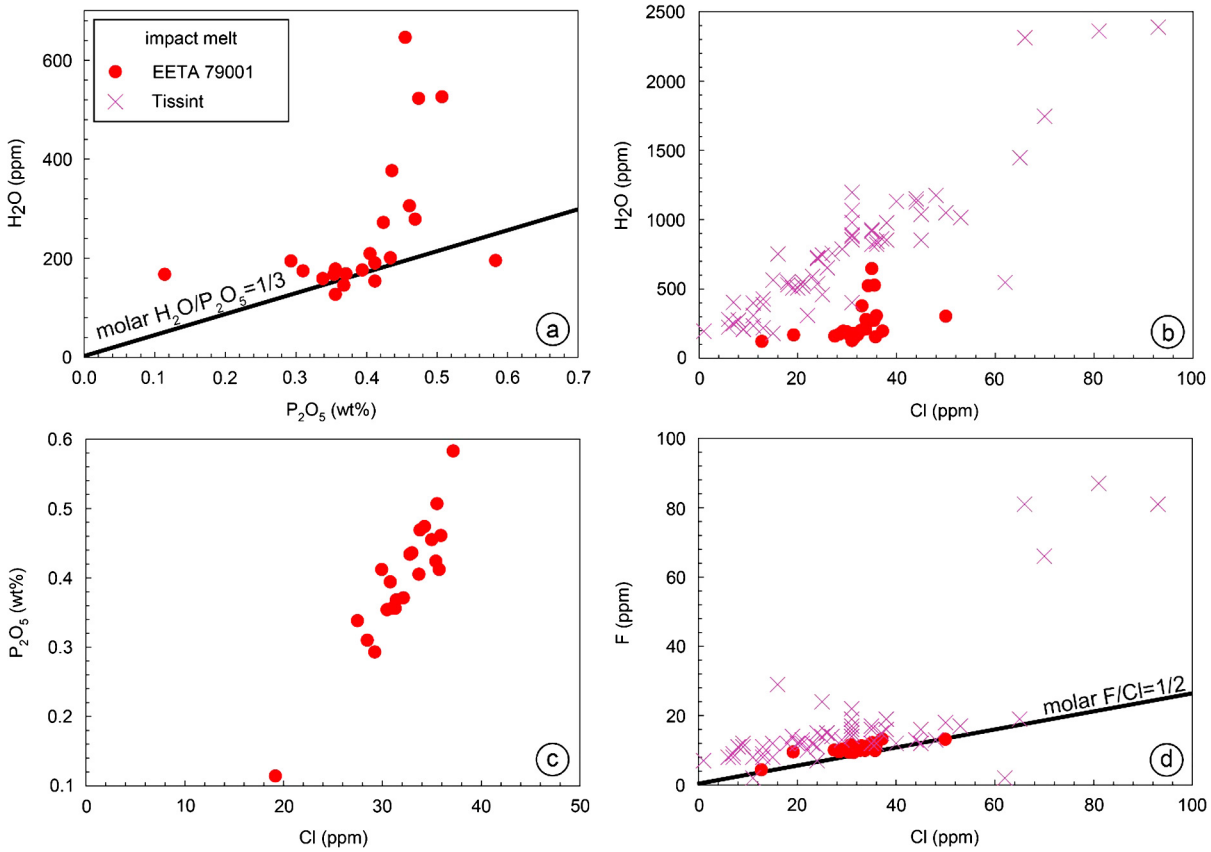

Fig. 4. Positive correlations between H_2O, F, Cl, and P_2O_5 in the impact melts in EETA 79001, compared to those in Tissint (Chen et al., 2015a). a: Molar $H_2O/P_2O_5 \geq 1/3$, indicating that apatite cannot be the sole source for the H_2O. b: The impact melts in EETA 79001 have less variation in H_2O and Cl compared to that in Tissint. At similar Cl concentrations, the impact melts in EETA 79001 have less H_2O than Tissint. c: Cl and P_2O_5 in the impact melts in EETA 79001 are positively correlated. d: F and Cl in the impact melts in EETA 79001 and Tissint are positively correlated. The F/Cl values were not strongly fractionated during impact melting and mixing. F/Cl in the impact melts in EETA 79001 is 0.5, and that in Tissint is between 0.5 and 1.

different samples do not show distinct difference in other volatile concentrations. Volatile concentrations are positively (but not linearly) correlated between H_2O, F, Cl, and P_2O_5 with much scatter (Fig. 4). The δD values in the impact melts vary from +3368 to +4639‰, and show a weak correlation with H_2O or other volatile concentrations (Fig. 3a). There is no difference in δD between impact melts and veins in different samples.

3.4. Estimation of C contents in impact melts

We also report SIMS $^{12}C^-/^{18}O^-$ values (after background removal) in olivine, maskelynite/feldspathic glass, merrillite, and impact melts (Tables S3–S6). The olivine analysis in sample 715 (indium mount) has a $^{12}C^-/^{18}O^-$ value of 5.77×10^{-4} (Table S3). The maskelynite grains in both epoxy and indium mounted samples have the lowest $^{12}C^-/^{18}O^-$ values ($6.7–9.8 \times 10^{-5}$, Table S4). The impact melt pockets and veins have about ten-times more $^{12}C^-/^{18}O^-$ than maskelynite ($2.53–13.5 \times 10^{-4}$, Table S6). Merrillite analysis has $^{12}C^-/^{18}O^-$ values between 1.22 and 21.7×10^{-4} (Table S5). Although olivine and merrillite display $^{12}C^-/^{18}O^-$ values similar to those of impact melts, their carbon concentrations may be different due to non-negligible matrix effect. We did not perform calibration for the carbon concentrations in this study. Using SIMS calibration coefficients from previous sessions on glass in the Tissint study (Chen et al., 2015a), the equivalent CO_2 concentrations in EETA maskelynite are 2–3 ppm, and those in the impact melts are 7–38 ppm. The uncertainty of these estimates is about 30% relative, based on the variability of the calibration coefficients across different SIMS sessions. In comparison, the phases in the Tissint meteorite contain more CO_2 with 7–20 ppm CO_2 in maskelynite and 8–173 ppm CO_2 in impact melts (Chen et al., 2015a).

4. Discussion

Below we will first compare our data to previous studies, discuss the chemical and isotopic changes of minerals in or next to impact melts, and then analyze the possible volatile sources recorded by EETA 79001 impact melts. Finally, we will compare EETA 79001 to Tissint by Chen et al. (2015a) and to LAR 06319 by Usui et al. (2015) and discuss the differences and similarities of water sources recorded in these meteorites.

4.1. Comparison with the literature data of impact melts and minerals in EETA 79001

Volatiles in impact melts and minerals in EETA 79001 were previously studied by Boctor et al. (2003) and Usui et al. (2015). Boctor et al. (2003) studied impact melts and minerals from Lithology C and the olivine-free basaltic portion of EETA 79001. Usui et al. (2015) analyzed an impact melt in maskelynite in Lithology A. Results of impact melts by Boctor et al. (2003) and Usui et al. (2015) are systematically offset toward higher H_2O contents (smaller $1/H_2O$) and lower δD values. Maskelynite and pyroxenes by Boctor et al. (2003) also display higher H_2O and lower δD values than our data (Fig. 3b). Boctor et al. (2003) suggested that the scattering in their data indicates terrestrial contamination in the SIMS analysis, which is consistent with the systematic difference compared to data in this study. However, Boctor et al. (2003) did

not report elemental chemistry and textural context of the analyzed points, which precludes a detailed analysis of causes for the differences.

Usui et al. (2015) reported two points of a maskelynite-hosted impact melt with δD of +1454 to +1644‰. From these values, they argued that the subsurface water source did not equilibrate with the present-day atmosphere, and proposed the existence of heterogeneous subsurface water reservoirs. As shown in Boctor et al. (2003) and Chen et al. (2015a), volatiles in impact melts vary significantly among different impact melts, depending on the proportions of magmatic minerals and alteration materials mixed by the impact melting process. As such, the use of impact melts to infer the nature of volatile sources requires a sufficient number of analyses. Two data points by Usui et al. (2015) do not produce a meaningful fit for subsurface water chemistry. In addition, the impact melt data by Usui et al. (2015) display unusually high C contents (254 and 445 ppm CO_2) relative to our analysis of 7–38 ppm for EETA 79001 (see above), in addition to lower δD values than our analysis. Thus, although the samples in Usui et al. (2015) were prepared without water, we speculate that terrestrial contamination cannot be fully ruled out. For the following discussion, we only use data of EETA 79001 from this study, because of the larger number of internally consistent analyses.

4.2. Chemical effects of shock on minerals in or near melt pockets

An interesting finding in our data is chemical effects of impact melt on minerals. Maskelynite/feldspathic glass and pyroxene grains in or in contact to the impact melts contain larger D/H values and sometimes higher H than those away from impact melts (Fig. 3a). Merrillite grains next to impact melts show compositional zonation whereas those away do not (Fig. 2). These observations highlight the need of petrography context in explaining the mineral SIMS-H data.

4.2.1. D and H changes in maskelynite/feldspathic glass and pyroxene near impact melts

The large D/H values and enriched H in maskelynite/feldspathic glass and pyroxenes in or next to impact melts are uncharacteristic for these magmatic phases, because the magmatic volatile abundances are typically low in both values (Boctor et al., 2003; Chen et al., 2015a; Mane et al., 2016).

We evaluate diffusive in-gassing from impact melt as a possible mechanism to enrich D and H in maskelynite and pyroxenes in or in contact with impact melts. A comprehensive analysis will require knowledge of diffusivities of D and H in mineral and basaltic melt, and partition coefficients of D and H between mineral and melt. Since the diffusivity for D is unknown, the following evaluation focuses on the H diffusion and partitioning. There would be a large chemical and thermal gradient between impact melts (100's ppm of H_2O with D/H $\approx 6 \times$ VSMOW, T $\gg 1000\,^{\circ}C$) and the original NAMs (10's ppm of H_2O with D/H $\approx$ VSMOW, T $< 100\,^{\circ}C$). For the rock next to the impact melt, it takes a few seconds to cool down from the supra-liquidus temperature, since the majority of the rock host remains at its original temperature (e.g., Shaw and Walton, 2013). At a spatial scale of ~20 μm (size of the grain or distance from the contact, Fig. S5), diffusion would take 1–10 s to significantly alter H_2O content, estimated using the square-root law [$x = (Dt)^{0.5}$], H_2O diffusivity in basaltic melt at 1500 °C (Y. Zhang et al., 2007; L. Zhang et al., 2017), and assuming a water content of 100 ppm. This duration fits with the estimated cooling time-scale for phases adjacent to large pockets (Shaw and Walton, 2013). However, for two maskelynite with high D/H and H contents (524-7 and 524-11, Table S4) at ~200 μm away from impact melt, diffusion is too slow (~1000 s) to change H contents before the host cools down to solidus within 5 s (Shaw and Walton, 2013). Rather, it is possible that shock locally devolatilized water from hydrous alteration products, which was subsequently trapped by shocked minerals (Tyburczy et al., 1990, 2001; Minitti et al., 2008a, 2008b). The shock experiments on amphiboles with 0.8 to 1.25 wt% H_2O by Minitti et al. (2008a, 2008b) demonstrated that water vapor in the shock chamber and from the target minerals can be implanted into these OH-bearing minerals. The ability to trap devolatilized vapor may be mineral dependent, considering that pre-shock plagioclase and pyroxene are cleavage-bearing compared to olivine that are typically free of cleavages.

We also note that olivine in impact melt pockets lacks H and D enrichment. Hydrogen diffusion in olivine is faster than in pyroxene (Kohlstedt and Mackwell, 1998; Hercule and Ingrin, 1999), but olivine holds less H than pyroxene (Aubaud et al., 2004). Hence, the bulk H diffusivity in olivine–pyroxene mixture is closer to that in pyroxene, about 8×10^{-11} m^2/s at 1300 °C (Zhang and Liu, 2012). Therefore, the lack of H enrichment likely reflects less partition of H and D in olivine.

4.2.2. Effects on merrillite

The compositional zoning in merrillite was observed only in grains in or next to impact melts, suggesting impact melts played a role in altering these grains. This is the first report of such effects on merrillite, although a previous study reported local devolatilization of apatite by invading impact melt veins in NWA 7755 (Howarth et al., 2015). The different zonation in Na and Mg cannot be simply explained by diffusive exchange between merrillite and impact melts. Rather, the zonation in merrillite grains is likely formed by impact-melts-induced dissolution and re-precipitation of merrillite. During impact heating, a portion of the merrillite was dissolved into the melt, producing a mixed melt with high P concentration and low Na concentration. As the melt cools down, merrillite would become oversaturated and grow rapidly onto the existing grain. Because of the mixing between merrillite and silicate melt, the newly grown merrillite would contain lower Na. The dissolution and quench growth rates are often faster than diffusion rates in minerals. For example, Zhang (2008) showed that dissolution distance is 48 μm while diffusion distance is only about 1 μm in olivine (Fig. 4-18 in Zhang, 2008). Quench growth rims are common in experimental studies (e.g., Zhang et al., 1989; Yu et al., 2016). Therefore, for impact melts that reach above the liquidus temperature (as most of the surrounding rock was molten), the dissolution and then quench growth should work more efficiently.

The H contents and D/H values from the center of merrillite grains show no correlation with their distances from impact melts (Table S5). Merrillite grains next to impact melts are 20–25 μm wide (Fig. 2), and the processes affecting silicate grains would have been effective. However, because merrillite grains contain similar amounts of H as impact melts, it would require longer time or more shock-induced vapor to alter D/H values in merrillite grains than maskelynite and pyroxene grains. A further implication is that impact melts are inefficient in changing H and D compositions of a mineral when the OH content of the mineral is similar to or higher than the impact melt.

4.3. Volatile sources recorded in EETA 79001 impact melt pockets

The generally negative and linear correlation between δD and 1/H_2O and the positive correlations between H_2O, F, Cl, and P in the impact melts (Figs. 3 and 4) are most consistent with mixing of two endmembers, each representing a distinct volatile source. A detailed assessment of how to disentangle these two sources was presented in Chen et al. (2015a) for Tissint melt pockets. The reasoning is equally applicable to EETA 79001 melt pockets.

One endmember has low H_2O, F, Cl, and P concentrations, and low δD values. Considering the lower volatile concentrations and the association of these features with the silicate minerals far from impact melts, this source is attributed to magmatic volatiles stored in minerals of the pre-impact rocks ('magmatic source'). As discussed in Chen et al. (2015a), inference of the exact H_2O content of pre-impact rock requires knowledge of the magmatic δD value and vice versa. From the fit of impact melt data, the H_2O content in the pre-impact rock for EETA 79001 is $\sim$10 $\pm$ 2 ppm with δD of 0 to $-$100‰. The low δD value is guided by the values in maskelynite and olivines, and is consistent with the suggestion for Tissint (Chen et al., 2015a; Mane et al., 2016).

The other endmember is characterized by high H_2O, F, Cl, and P contents, and a high δD value of about +5000‰. Chen et al. (2015a) conducted a detailed assessment of all potential sources, and deduced that subsurface alteration materials present in the pre-shock vesicles are the most likely source for this endmember. The pre-shock vesicles provided a pathway for fluids, which likely equilibrated with Martian atmosphere and picked up halogens from soils. We emphasize that direct atmosphere implantation by shock is inconsistent with the observations because of lower CO_2/H_2O ratios (<0.1) in impact melt pockets than in the present-day Martian atmosphere (>6000, e.g., Mahaffy et al., 2013). In EETA melt pockets, H_2O is more abundant than CO_2. In Tissint melt pockets, H_2O content (in wt%) is a factor of 10 to 75 times higher than that of CO_2, except for a point on a bubble (Chen et al., 2015a). Current Martian atmosphere is dominantly CO_2 with trace amounts of water (95 vol% CO_2, 1.93 vol% Ar, and 0.015 vol% H_2O, e.g., Mahaffy et al., 2013). Although the amount of H_2O vapor varies with latitudes and seasons (e.g., 0–70 ppmv in northern spring, 0–250 ppmv in northern late spring), water vapor is still a trace component of the present-day atmosphere (e.g., Villanueva et al., 2015). If the Martian atmosphere were directly implanted, we would expect CO_2 contents to be much higher than H_2O, even after considering the different solubility (e.g., Liu et al., 2005; Y. Zhang et al., 2007). The Martian climate changes with the oscillating obliquity of Mars at a timescale of 10^5 to 10^6 yrs and water vapor pressure in the Martian atmosphere may be high enough to reach saturation at high obliquity (e.g., Jakosky and Carr, 1985). However, it would be highly serendipitous that shergottites launched by different impacts from $\sim$19 Ma to 0.7 Ma always occurred at high obliquity. Furthermore, the positively correlated H_2O and halogens cannot be explained by direct atmosphere implantation. Another suggestion is subsurface water or water ice in pre-shock vesicles (Usui et al., 2015). However, this suggestion is not consistent with atmosphere-like noble gas isotopes in impact melt pockets (e.g., Bogard and Johnson, 1983), because the Martian atmosphere would have been pushed out by water or water ice (Wiens, 1988). Therefore, pre-shock vesicles contain either water frost or subsurface alteration. The subsurface water source displays a δD of +4200‰, based on the intercept of the δD and $1/H_2O$ trend at y-axis (δD, Fig. 3a). Considering the scattering, the δD-intercept of the trend ranges from +4000‰ to +5000‰, similar to present day atmosphere of +4950 $\pm$ 1080‰ (Fig. 3b). On the basis of the $\sim$170 Ma crystallization age and $\sim$0.7 Ma cosmic-ray exposure age, volatiles in EETA 79001 impact melts indicate the pre-shock rock experienced subsurface fluid alterations, similar to Tissint.

4.4. Volatile sources recorded in EETA 79001 merrillite

It is interesting to note that merrillite data also form a mixing trend, but the trend differs from that of melt pockets and maskelynite. The δD and $1/H_2O$ trend extends to a similar subsurface source, but the magmatic source contains a higher H_2O content than that inferred from impact melts and maskelynite (Fig. 3a). Recently, Adcock et al. (2017) reported that 'merrillite' in Martian meteorites may be produced by shock transformation of whitlockite. As discussed above, the δD and $1/H_2O$ variations is not caused by the proximity of these grains to impact melts, nor follow a degassing trend. The total range of 2000‰ variation in δD is much larger than those observed in previous shock experiments on hydrous minerals (e.g., <30‰ for $\sim$12% volatile loss, Tyburczy et al., 1990). Therefore, shock is unlikely to be the main cause of δD and H_2O variation in merrillite. Rather, the increase in δD with H_2O contents of merrillite implies that some merrillite may have experienced post-crystallization metasomatic alteration by subsurface fluids, similar to those observed in apatite (Howarth et al., 2016). Alternatively, the δD and H_2O trend of merrillite may reflect merrillite formation during late-stage assimilation of Martian crust (Greenwood et al., 2008). The magmatic volatile contents of pre-alteration merrillite is $\sim$55 ppm, if we assume the magmatic δD is similar to 0 to $-$100‰ as in silicates.

4.5. Comparison to impact melt data in other Martian meteorites

Volatile contents in impact melts have only been studied in three meteorites (Fig. 5), including Tissint (Chen et al., 2015a; Kuchka et al., 2017), EETA 79001 (Boctor et al., 2003; Usui et al., 2015; this study), and LAR 06319 (Usui et al., 2015). The ejection age, crystallization age, and chemical characteristics of these three meteorites are sufficiently different (see below). Therefore, differences and similarities between volatile sources derived from impact melts of three samples provide important insights in the crustal and mantle processes.

4.5.1. Subsurface water chemistry in Martian meteorites and clay minerals

Subsurface water inferred from EETA 79001, LAR 06319, and Tissint has a similar hydrogen isotope composition (+4000 to +5000‰, Fig. 5b). EETA 79001 and Tissint have similar cosmic-ray exposure aged of $\sim$0.7 and 1 Myrs, respectively (Nyquist et al., 2001; Chennaoui Aoudjehane et al., 2012). LAR 06319 has a cosmic ray exposure age of $\sim$3.3 Ma from an older impact event (Nagao and Park, 2008). Crystallization ages of these three meteorites increase from $\sim$170 Ma for EETA 79001, to $\sim$190 Ma for LAR 06319, to $\sim$600 Ma for Tissint (Nyquist et al., 2001; Shafer et al., 2010; Brennecka et al., 2014). Therefore, Tissint had more chance to have experience aqueous alteration than LAR 06319 and EETA 79001. The similar δD values of the subsurface sources among these three samples indicate that the D/H values of the subsurface fluids are similar for the crustal areas, from which these three samples were ejected. Thus, the fluid D/H chemistry appears to be stable from $\sim$600 Ma to present.

As mentioned above, the amount of initial water on Mars is estimated largely from few data points. Villanueva et al. (2015) suggested that initial water has a global equivalent layer >137 m deep, estimated from Rayleigh distillation model, and D/H values of the present-day Martian atmosphere (Webster et al., 2013) and polar ice. Kurokawa et al. (2014) conducted a two-stage water loss model, with initial rapid loss of Martian water between 4.5 Ga (assumed δD to be magmatic water from melt inclusion in Yamato 980459, 275‰, Usui et al., 2012) and 3 Ga (clay minerals in a mudstone at Gale crater, δD = +3000‰, Mahaffy et al., 2015), and a slower loss from 3 Ga to present-day (Martina atmosphere, δD = +5000‰ at 0 Ga, Webster et al., 2013). Kurokawa et al. (2014) estimated initial water has a global equivalent layer of >41 to 152 m deep. These models provide a lower limit of initial water amount since D/H values and the amount of subsurface water reservoir are unknown. Rather than continuous loss assumed in these models, our finding of similar subsurface water chemistry since 600 Ma implies that surface water may be replenished from

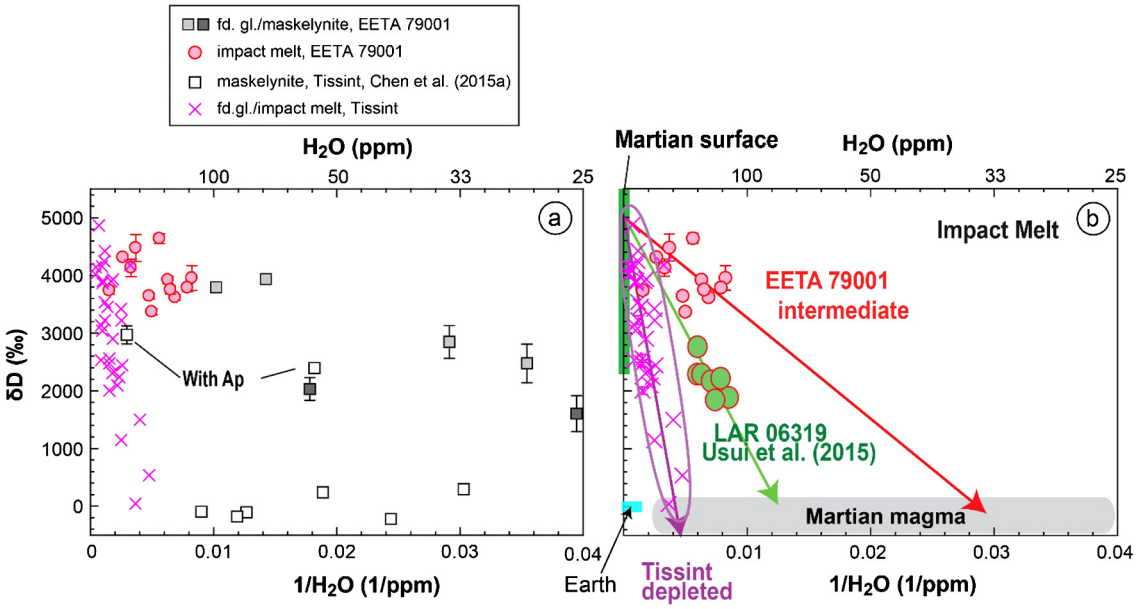

Fig. 5. Comparison of EETA 79001 to Tissint and LAR 06319. (a) Comparison of impact melt, feldspathic glass, and maskelynite in EETA 79001 with those in Tissint from Chen et al. (2015a). Note that feldspathic glass (fd. gl.) was included as impact melts in Chen et al. (2015a). (b) Comparison of subsurface and magmatic sources inferred from impact melts among enriched shergottite LAR 06319 (data from Usui et al., 2015), intermediate shergottite EETA 79001 (this study), and depleted shergottite Tissint (Chen et al., 2015a).

groundwater, and thus the amount of water loss could be larger than expected.

4.5.2. Magmatic water in shergottites of different chemical signatures

We found that water contents in the magmatic endmember decrease from Tissint (−200 ppm) to LAR 06319 (∼77 ppm) to EETA 79001 (∼10 ppm, Fig. 5b), opposite to the prediction based on apatite compositions (McCubbin et al., 2016). The discrepant results between two different methods do not suggest one or the other methodology is falsified. For apatite, the OH content of the mantle source was calculated using estimated OH and measured F contents in apatite from EPMA, experimental F–OH distribution coefficients between apatite and melt, bulk-rock F contents, and assumed degrees of partial melting (e.g., McCubbin et al., 2016). The F/OH ratio is less susceptible to fractionation, but can be affected by degassing, or assimilation, or post-crystallization fluid interaction that occur red between the partial melt from the mantle and the melt that formed apatite, or post-crystallization fluid interaction (e.g., Greenwood et al., 2008; Howarth et al., 2016).

The OH contents in pre-impact rock reflect the melt OH contents from which the constituent phases crystallized. Although Tissint is derived from mantle sources depleted in incompatible elements, the higher FeO/MgO and higher abundances of rare earth elements suggest its parental melt is more evolved (or fractionated) than other depleted shergottites (e.g., Liu et al., 2016). As a result, the OH content of pre-impact Tissint may be enriched because of the higher degree of crystal fractionation from the primitive melt than other depleted shergottites. For LAR 06319 from a mantle source that is enriched in incompatible trace elements compared to Tissint, fractionation of the primitive melt may lead to volatile saturation and degassing before the formation of pre-impact rock. The lowest water content in EETA 79001 indicates a complex history that may involve longer residence at different depths, additional degassing, or multiple impacts. Part of this complexity was found in the mineral chemistry and texture, and the crystallization involved assimilation of Mg-rich olivine and orthopyroxene by depleted melt, followed by crystallization under progressive decompression (e.g., Liu et al., 2013). The lower water content of the magmatic source in EETA 79001 is also recorded in its maskelynite data. Such comparison with LAR 06319 cannot be made since maskelynite in LAR 06319 has not been analyzed. The H_2O concentrations in the maskelynite in EETA 79001 that are least affected by impact melts are <10 ppm, whereas those in Tissint range from 33–100 ppm with consistently low δD values.

5. Conclusions

We measured major-element compositions, volatile concentrations (including H reported as H_2O, F, Cl, P, and S), and hydrogen isotope compositions in the impact melts, maskelynite, pyroxene, olivine, and merrillite in Martian meteorite EETA 79001. New findings of this study include that merrillite inside or close to impact melts are zoned in Na and Mg, and nominally anhydrous minerals enclosed in impact melts are enriched in D and contain noticeable volatiles that are otherwise depleted in those away from impact melts. The effect of impact melt on D/H of relatively OH-rich merrillite, however, is not discernable in the available data. This observation suggests that cautions need to be exercised when use D/H value and OH contents of NAMs without the textural information.

The concentrations of H_2O and hydrogen isotope compositions of impact melts and feldspathic glass in or near impact melts are positively correlated with each other. Together with positive correlations between H_2O, F, Cl, and P, these results indicate mixing between a volatile-rich, high-δD source and a volatile-poor, low-δD source. The volatile-rich source contains high amounts of H_2O, F, and Cl and large δD value that is consistent with a subsurface source equilibrated with the present-day atmosphere. The δD value of the subsurface source in EETA 79001 (∼+4200‰) is similar to those inferred from impact melts in Tissint and LAR 06319, even though they have different crystallization ages and ejection ages. The similar δD values in subsurface water indicate that chemistry of subsurface fluid remained stable for the last 600 Myrs. Our results do not support a previous suggestion of an isotopically distinct subsurface water reservoir with a δD value of +1000 to +2000‰ in EETA 79001 compared to Tissint with a δD value of +4000 to +5000‰.

The volatile-poor, low-δD source was volatiles contained in the pre-shock rock. The inferred H_2O content for EETA is ∼10 ppm,

drier than that inferred for the Tissint (∼200 ppm) and LAR 06319 (∼100 ppm). The contrast in pre-shock water contents among three samples is consistent with the fact that these basaltic meteorites experienced different degrees of differentiation and/or assimilation.

Acknowledgements

This work was largely conducted at the Jet Propulsion Laboratory, which is managed by the California Institute of Technology (Caltech) under a contract with NASA. We thank constructive reviews from T. Usui and A. Udry. YL thanks the support from JPL-Caltech President's and Director's Fund and partial support by NASA Cosmochemistry grant NNN13D465T. We thank the Johnson Space Center Meteorite Working Group for allocating the samples. The EPMA and SEM were performed at the Caltech Geological and Planetary Science Division Analytical Facility, which is supported in part by NSF grants EAR-0318518 and DMR-00800065. SIMS analysis was done at the Caltech Microanalysis Center that is partially supported by the Gordon and Betty Moore Foundation.

Appendix A. Supplementary material

Supplementary material related to this article can be found online at https://doi.org/10.1016/j.epsl.2018.03.019.

References

Adcock, C.T., Tschauner, O., Hausrath, E.M., Udry, A., Luo, S.N., Cai, Y., Ren, M., Lanzirotti, A., Newville, M., Kunz, M., Lin, C., 2017. Shock-transformation of whitlockite to merrillite and the implications for meteoritic phosphate. Nat. Commun. 8, 14667.

Anovitz, L.M., Riciputi, L.R., Cole, D.R., Fayek, M., Elam, J.M., 2006. Obsidian hydration: a new paleothermometer. Geology 34, 517–520.

Aubaud, C., Hauri, E.H., Hirschmann, M.M., 2004. Hydrogen partition coefficients between nominally anhydrous minerals and basaltic melts. Geophys. Res. Lett. 31, L20611.

Beck, P., Ferroir, T., Gillet, P., 2007. Shock-induced compaction, melting, and entrapment of atmospheric gases in Martian meteorites. Geophys. Res. Lett. 34. https://doi.org/10.1029/2006gl028141.

Bibring, J.-P., Langevin, Y., Mustard, J.F., Poulet, F., Arvidson, R., et al., 2006. Global mineralogical and aqueous Mars history derived from OMEGA/Mars express data. Science 312, 400–404.

Boctor, N.Z., Alexander, C.M.O.D., Wang, J., Hauri, E., 2003. The sources of water in Martian meteorites: clues from hydrogen isotopes. Geochim. Cosmochim. Acta 67, 3971–3989.

Bogard, D.D., Johnson, P., 1983. Martian gases in an Antarctic meteorite? Science 221, 651–654.

Bogard, D.D., Nyquist, L.E., Johnson, P., 1984. Noble-gas contents of shergottites and implications for the Martian origin of SNC meteorites. Geochim. Cosmochim. Acta 48, 1723–1739.

Bogard, D., Hörz, F., Johnson, P., 1989. Shock-implanted noble gases II: additional experimental studies and recognition in naturally shocked terrestrial materials. Meteoritics 24, 113–123.

Boynton, W.V., Feldman, W.C., Squyres, S.W., Prettyman, T.H., Brückner, J., et al., 2002. Distribution of hydrogen in the near surface of Mars: evidence for subsurface ice deposits. Science 297, 81.

Brennecka, G.A., Borg, L.E., Wadhwa, M., 2014. Insights into the Martian mantle: the age and isotopics of the meteorite fall Tissint. Meteorit. Planet. Sci. 49, 412–418.

Carr, M.H., Head III, J.W., 2010. Geologic history of Mars. Earth Planet. Sci. Lett. 294, 185–203.

Chen, Y., Liu, Y., Guan, Y., Eiler, J.M., Ma, C., Rossman, G.R., Taylor, L.A., 2015a. Evidence in Tissint for recent subsurface water on Mars. Earth Planet. Sci. Lett. 425, 55–63.

Chen, Y., Zhang, Y., Liu, Y., Guan, Y., Eiler, J., Stolper, E.M., 2015b. Water, fluorine, and sulfur concentrations in the lunar mantle. Earth Planet. Sci. Lett. 427, 37–46.

Chennaoui Aoudjehane, H., Avice, G., Barrat, J.A., Boudouma, O., Chen, G., et al., 2012. Tissint Martian meteorite: a fresh look at the interior, surface, and atmosphere of Mars. Science 338, 785–788.

Crozaz, G., Floss, C., Wadhwa, M., 2003. Chemical alteration and REE mobilization in meteorites from hot and cold deserts. Geochim. Cosmochim. Acta 67, 4727–4741.

Gooding, J.L., Wentworth, S.J., Zolensky, M.E., 1991. Aqueous alteration of the Nakhla meteorite. Meteoritics 26, 135–143.

Greenwood, J.P., Itoh, S., Sakamoto, N., Vicenzi, E.P., Yurimoto, H., 2008. Hydrogen isotope evidence for loss of water from Mars through time. Geophys. Res. Lett. 35, L05203.

Hercule, S., Ingrin, J., 1999. Hydrogen in diopside: diffusion, kinetics of extraction-incorporation, and solubility. Am. Mineral. 84, 1577–1587.

Howarth, G.H., Pernet-Fisher, J.F., Bodnar, R.J., Taylor, L.A., 2015. Evidence for the exsolution of Cl-rich fluids in martian magmas: apatite petrogenesis in the enriched lherzolitic shergottite Northwest Africa 7755. Geochim. Cosmochim. Acta 166, 234–248.

Howarth, G.H., Liu, Y., Chen, Y., Pernet-Fisher, J.F., Taylor, L.A., 2016. Postcrystallization metasomatism in shergottites: evidence from the paired meteorites LAR 06319 and LAR 12011. Meteorit. Planet. Sci. 51, 2061–2072.

Hu, S., Lin, Y., Zhang, J., Hao, J., Feng, L., Xu, L., Yang, W., Yang, J., 2014. NanoSIMS analyses of apatite and melt inclusions in the GRV 020090 Martian meteorite: hydrogen isotope evidence for recent past underground hydrothermal activity on Mars. Geochim. Cosmochim. Acta 140, 321–333.

Jakosky, B.M., 1991. Mars volatile evolution: evidence from stable isotopes. Icarus 94, 14–31.

Jakosky, B.M., Carr, M.H., 1985. Possible precipitation of ice at low latitudes of Mars during periods of high obliquity. Nature 315, 559.

Jochum, K.P., Stoll, B., Herwig, K., Willbold, M., Hofmann, A.W., et al., 2006. MPI-DING reference glasses for in situ microanalysis: new reference values for element concentrations and isotope ratios. Geochem. Geophys. Geosyst. 7.

Jull, A.J.T., Donahue, D.J., 1988. Terrestrial 14C age of the Antarctic shergottite, EETA 79001. Geochim. Cosmochim. Acta 52, 1309–1311.

Kohlstedt, David L., Mackwell, Stephen J., 1998. Diffusion of hydrogen and intrinsic point defects in olivine. Z. Phys. Chem., 147.

Kovács, I., Green, D.H., Rosenthal, A., Hermann, J., O'Neill, H.S.C., et al., 2012. An experimental study of water in nominally anhydrous minerals in the upper mantle near the water-saturated solidus. J. Petrol. 53, 2067–2093.

Kuchka, C.R., Herd, C.D.K., Walton, E.L., Guan, Y., Liu, Y., 2017. Martian low-temperature alteration materials in shock-melt pockets in Tissint: constraints on their preservation in shergottite meteorites. Geochim. Cosmochim. Acta 210, 228–246.

Kurokawa, H., Sato, M., Ushioda, M., Matsuyama, T., Moriwaki, R., Dohm, J.M., Usui, T., 2014. Evolution of water reservoirs on Mars: constraints from hydrogen isotopes in martian meteorites. Earth Planet. Sci. Lett. 394, 179–185.

Liu, Y., Balta, J.B., Goodrich, C.A., McSween Jr., H.Y., Taylor, L.A., 2013. New constraints on the formation of shergottite Elephant Moraine 79001 lithology A. Geochim. Cosmochim. Acta 108, 1–20.

Liu, Y., Baziotis, I.P., Asimow, P.D., Bodnar, R.J., Taylor, L.A., 2016. Mineral chemistry of the Tissint meteorite: indications of two-stage crystallization in a closed system. Meteorit. Planet. Sci. 51, 2293–2315.

Liu, Y., Zhang, Y.X., Behrens, H., 2005. Solubility of H_2O in rhyolitic melts at low pressures and a new empirical model for mixed H_2O–CO_2 solubility in rhyolitic melts. J. Volcanol. Geotherm. Res. 143, 219–235.

Mahaffy, P.R., Webster, C.R., Atreya, S.K., Franz, H., Wong, M., et al., 2013. Abundance and isotopic composition of gases in the Martian atmosphere from the Curiosity rover. Science 341, 263–266.

Mahaffy, P.R., Webster, C.R., Stern, J.C., Brunner, A.E., Atreya, S.K., et al., 2015. The imprint of atmospheric evolution in the D/H of Hesperian clay minerals on Mars. Science 347, 412.

Mane, P., Hervig, R., Wadhwa, M., Garvie, L.A.J., Balta, J.B., McSween, H.Y., 2016. Hydrogen isotopic composition of the Martian mantle inferred from the newest Martian meteorite fall, Tissint. Meteorit. Planet. Sci. 51, 2073–2091.

McCubbin, F.M., Boyce, J.W., Srinivasan, P., Santos, A.R., Elardo, S.M., Filiberto, J., Steele, A., Shearer, C.K., 2016. Heterogeneous distribution of H_2O in the Martian interior: implications for the abundance of H_2O in depleted and enriched mantle sources. Meteorit. Planet. Sci.

Minitti, M.E., Rutherford, M.J., Taylor, B.E., Dyar, M.D., Schultz, P.H., 2008a. Assessment of shock effects on amphibole water contents and hydrogen isotope compositions: 1. Amphibolite experiments. Earth Planet. Sci. Lett. 266, 46–60.

Minitti, M.E., Leshin, L.A., Dyar, M.D., Ahrens, T.J., Guan, Y., Luo, S.-N., 2008b. Assessment of shock effects on amphibole water contents and hydrogen isotope compositions: 2. Kaersutitic amphibole experiments. Earth Planet. Sci. Lett. 266, 288–302.

Nagao, K., Park, J., 2008. Noble gases and cosmic-ray exposure ages of two Martian shergottites, RBT 04262 and LAR 06319, recovered in Antarctica. In: 71st Annual Meteoritical Society Meeting. #5200.

Nyquist, L.E., Bogard, D.D., Shih, C.Y., Greshake, A., Stoffler, D., Eugster, O., 2001. Ages and geologic histories of Martian meteorites. Space Sci. Rev. 96, 105–164.

Owen, T., Maillard, J.P., de Bergh, C., Lutz, B.L., 1988. Deuterium on Mars: the abundance of HDO and the value of D/H. Science 240, 1767.

Rauch, M., Keppler, H., 2002. Water solubility in orthopyroxene. Contrib. Mineral. Petrol. 143, 525–536.

Shafer, J.T., Brandon, A.D., Lapen, T.J., Righter, M., Peslier, A.H., Beard, B.L., 2010. Trace element systematics and ^{147}Sm–^{143}Nd and ^{176}Lu–^{176}Hf ages of Larkman Nunatak 06319: closed-system fractional crystallization of an enriched shergottite magma. Geochim. Cosmochim. Acta 74, 7307–7328.

Shaw, C.S.J., Walton, E., 2013. Thermal modeling of shock melts in Martian meteorites: implications for preserving Martian atmospheric signatures and crystallization of high-pressure minerals from shock melts. Meteorit. Planet. Sci. 48, 758–770.

Treiman, A.H., Barrett, R.A., Gooding, J.L., 1993. Preterrestrial aqueous alteration of the Lafayette (SNC) meteorite. Meteoritics 28, 86–97.

Tyburczy, J.A., Krishnamurthy, R.V., Epstein, S., Ahrens, T.J., 1990. Impact-induced devolatilization and hydrogen isotopic fractionation of serpentine: implications for planetary accretion. Earth Planet. Sci. Lett. 98, 245–261.

Tyburczy, J.A., Xu, X., Ahrens, T.J., Epstein, S., 2001. Shock-induced devolatilization and isotopic fractionation of H and C from Murchison meteorite: some implications for planetary accretion. Earth Planet. Sci. Lett. 192, 23–30.

Usui, T., Alexander, C.M.O.D., Wang, J., Simon, J.I., Jones, J.H., 2012. Origin of water and mantle–crust interactions on Mars inferred from hydrogen isotopes and volatile element abundances of olivine-hosted melt inclusions of primitive shergottites. Earth Planet. Sci. Lett. 357–358, 119–129.

Usui, T., Alexander, C.M.O.D., Wang, J., Simon, J.I., Jones, J.H., 2015. Meteoritic evidence for a previously unrecognized hydrogen reservoir on Mars. Earth Planet. Sci. Lett. 410, 140–151.

Villanueva, G.L., Mumma, M.J., Novak, R.E., Käufl, H.U., Hartogh, P., Encrenaz, T., Tokunaga, A., Khayat, A., Smith, M.D., 2015. Strong water isotopic anomalies in the martian atmosphere: probing current and ancient reservoirs. Science 348, 218.

Walton, E.L., Shaw, C.S.J., 2009. Understanding the textures and origin of shock melt pockets in Martian meteorites from petrographic studies, comparisons with terrestrial mantle xenoliths, and experimental studies. Meteorit. Planet. Sci. 44, 55–76.

Webster, C.R., Mahaffy, P.R., Flesch, G.J., Niles, P.B., Jones, J.H., Leshin, L.A., Atreya, S.K., Stern, J.C., Christensen, L.E., Owen, T., Franz, H., Pepin, R.O., Steele, A., Team, t.M.S., 2013. Isotope ratios of H, C, and O in CO_2 and H_2O of the Martian atmosphere. Science 341, 260–263.

Wiens, R.C., 1988. On the siting of gases shock-emplaced from internal cavities in basalt. Geochim. Cosmochim. Acta 52, 2775–2783.

Wiens, R.C., Pepin, R.O., 1988. Laboratory shock emplacement of noble gases, nitrogen, and carbon dioxide into basalt, and implications for trapped gases in shergottite EETA 79001. Geochim. Cosmochim. Acta 52, 295–307.

Yu, Y., Zhang, Y., Chen, Y., Xu, Z., 2016. Kinetics of anorthite dissolution in basaltic melt. Geochim. Cosmochim. Acta 179, 257–274.

Zhang, L., Guo, X., Wang, Q., Ding, J., Ni, H., 2017. Diffusion of hydrous species in model basaltic melt. Geochim. Cosmochim. Acta 215, 377–386.

Zhang, Y.X., 2008. Geochemical Kinetics. Princeton University Press.

Zhang, Y., Liu, L., 2012. On diffusion in heterogeneous media. Am. J. Sci. 312, 1028–1047.

Zhang, Y., Walker, D., Lesher, C.E., 1989. Diffusive crystal dissolution. Contrib. Mineral. Petrol. 102, 492–513.

Zhang, Y., Xu, Z., Zhu, M., Wang, H., 2007. Silicate melt properties and volcanic eruptions. Rev. Geophys. 45, RG4004.

Impact-melt hygrometer for Mars: The case of shergottite Elephant Moraine (EETA) 79001

Yang Liu[a,*], Yang Chen[a], Yunbin Guan[b], Chi Ma[b], George R. Rossman[b], John M. Eiler[b], Youxue Zhang[c]

a: Jet Propulsion Laboratory, California Institute of Technology, Pasadena, CA 91109, USA
b: Division of Geological and Planetary Sciences, California Institute of Technology, Pasadena, CA 91125, USA
c: Department of Earth and Environmental Sciences, University of Michigan, Ann Arbor, MI 48109-1005, USA
*Corresponding author. Email: yang.liu@jpl.nasa.gov (Y. Liu)

Table of contents:

1. Supplementary Text

1.1 Analytical methods

The regions of interest were first examined using optical microscopy and scanning electron microscopy (SEM, ZEISS 1550VP and Hitachi SU3500) using instruments at Jet Propulsion Laboratory and California Institute of Technology (Caltech). After the volatile analysis using a Cameca secondary ion mass spectrometer (SIMS) IMS 7f-GEO at Caltech, the locations were examined again using SEM to ensure that they are on the intended targets and do not contain cracks or holes, which could contribute terrestrial contamination signals to SIMS data. For minerals next to impact melts, Raman analysis were also conducted to confirm their mineral structure.

The volatile concentrations and hydrogen isotopes were analyzed using the Cameca SIMS. We followed the previous procedures for SIMS analysis (Chen et al., 2015a,c) with special attention paid to minimize terrestrial contamination and to decrease the instrument background of hydrogen. A few days before analysis, the samples were cleaned in ethanol, coated with carbon, and placed in the high-vacuum sample storage chamber of the SIMS instrument. During analysis, the pressure in the sample chamber was 1-6 $\times$ 10^{-10} torr.

The analytical settings for the volatile concentrations in olivine, clinopyroxene, maskelynite, merrillite, impact melt pockets and veins are the same, except for the ion species and standards. Negative ion species were generated using a Cs^+ primary-ion beam. The beam current was 3-5 nA and the beam diameter was 15 μm. The field aperture size was 100 μm. Sample charging was compensated by an electron gun. A mass-resolving power (MRP) of ~5000 was used to distinguish $^{16}O^1H^-$ from $^{17}O^-$. Before and after each analysis, ion images of $^{12}C^-$ and $^{16}O^1H^-$ were examined to check for contamination signals. Each analysis position was pre-sputtered over an area of 25 $\times$ 25 μm for 2 minutes. The secondary ion $^{18}O^-$ was then automatically centered and mass-calibrated. The raster length was reduced to 2 $\times$ 2 μm during analysis. An electronic gating of 80-90% was used to exclude the secondary ions from the margins of the rastered area in order to avoid surface contamination. Each position was analyzed for 10-20 cycles. In each cycle, the counting time was 1 second for each ion species. Two natural olivine samples (0 and 3 ppm H_2O) were used to monitor and subtract the instrument background of hydrogen.

For olivine and clinopyroxene, five ion species, $^{12}C^-$, $^{16}O^1H^-$, $^{18}O^-$, $^{19}F^-$, and $^{30}Si^-$, were analyzed on EETA samples mounted in indium. Natural olivine and pyroxene samples were used for calibration. For merrillite, seven ion species, $^{12}C^-$, $^{16}O^1H^-$, $^{18}O^-$, $^{19}F^-$, $^{31}P^-$, $^{32}S^-$, and $^{35}Cl^-$, were analyzed and natural apatite samples were used as standards. For maskelynite and impact melt pockets and veins, eight ion species ($^{12}C^-$, $^{16}O^1H^-$, $^{18}O^-$, $^{19}F^-$, $^{30}Si^-$, $^{31}P^-$, $^{32}S^-$, and $^{35}Cl^-$) were analyzed. Natural volcanic glasses, MPI- DING glass standard (KL2-G, GOR128-G and GOR132-G, Jochum et al., 2006), and apatite were used for calibration (Table S2). In this study, the H_2O contents of all MPI-DING glass standards except for BM90/21-G were determined directly using Fourier Transform InfraRed spectroscopy (FTIR). The H_2O contents of quartz dioritic, basaltic and andesitic glasses are 0.34 to 0.65 of the informative values in Jochum et al. (2006), whereas a rhyolitic glass is ~2.34 times higher (Table S2). We used the FTIR contents for SIMS calibration. The SIMS measurements in Chen et al. (2015a, b, c) and Kuchka et al. (2017) also used these standards and the FTIR-determined H_2O contents.

Hydrogen isotopes ($^1H^-$ and D^-) were analyzed using similar beam conditions as for the volatile concentrations, except for a MRP of 500~800. Before and after each analysis, ion images of $^1H^-$ were examined to check contamination signals. After pre-sputtering, the secondary ion $^1H^-$ was manually centered and mass-calibrated. Each position was analyzed for

50-100 cycles, depending on the hydrogen abundance. In each cycle, the counting time was 1 second for $^{1}H^{-}$ and 15 seconds for $^{2}H^{-}$. The instrument fractionation factors for $^{2}H^{-}/^{1}H^{-}$ were 0.91 and 1.02 in two separated analysis sessions, determined using a natural volcanic glass (see the supplementary file). All reported data are corrected for instrument fractionation and background.

The SIMS uncertainties (2σ) are 20% relative for H_2O, P_2O_5, and S, and 10% relative for F and Cl, based on the reproducibility of the standards. The uncertainties (2σ) for the δD values are from 47 to 423 ‰ (Tables S3-S6). The instrument backgrounds are 4-8 ppm for H_2O, 1 ppm for F, 0.3 ppm for P_2O_5, and 0.1 ppm for S and Cl, based on the apparent concentrations in olivine grains (Tables S3-S6). Reported volatile contents have been corrected for the background values.

The major element compositions of the phases were analyzed using electron probe micro-analysis (EPMA, JEOL JXA-8200) at Caltech, with an electron beam of 15 kV, 10-25 nA, and a 5 μm diameter. Two merrillite grains were repeatedly analyzed with different beam current and diameter (10-25 nA beam current, focused beam to 10 μm diameter beam), and no beam sensitivity was observed. The counting times for each element were 20 seconds on peak and 10 seconds on each background. The analytical uncertainties and detection limits are listed in Table S3-S6. In addition, Na *K*α, Mg *K*α, Fe *K*α, Ca *K*α, and Cl *K*α X-ray maps of three merrillite grains were collected using EPMA with a focused beam of 15 kV and 10 nA.

1.2 FTIR analysis of MPI-DING glasses

Two random fragments of MPI-DING glasses GOR128-G, GOR 132-G, and KL2-G, and one fragment of ML3B-G, T1-G, StHs/80-G, and ATHO, were obtained from MPI. These chips were doubly polished to generate two parallel surfaces.

Water concentrations of these chips were analyzed using a microscope unit of a PerkinElmer GX FTIR spectrometer at the University of Michigan. We used a visible source, a CaF_2 beamsplitter, a liquid N_2 cooled MCT detector, a slit aperture of 50 x 50 μm, and 128 or 256 scans. To minimize the interference of atmospheric H_2O, samples are under dry N_2 flow and a new background was taken before each sample. Three to four different locations on the polished glass chips were analyzed to check homogeneity, which is reflected by the 2 standard deviation of the average.

The absorbance at ~3550 cm^{-1} band was measured after correcting the continuum background (straight baseline). Water concentrations were calculated using the Beer-Lambert law and molar absorption coefficients in Table S2. Results show that water contents in basaltic and dacitic glasses are ~0.3-0.6 times the informative values in Jochum et al. (2006), and that in rhyolitic glass is about 2.34 times the information value.

References:

Chen, Y., Liu, Y., Guan, Y., Eiler, J.M., Ma, C., Rossman, G.R., Taylor, L.A., 2015a. Evidence in Tissint for recent subsurface water on Mars. Earth Planet. Sci. Lett. 425, 55-63.

Chen, Y., Liu, Y., Guan, Y., Eiler, J.M., Ma, C., Rossman, G.R., 2015b. Surface and magmatic water signatures in EETA 79001 impact melts. 46th Lunar and Planetary Science Conference, #2291.

Chen, Y., Zhang, Y., Liu, Y., Guan, Y., Eiler, J., Stolper, E.M., 2015c. Water, fluorine, and sulfur concentrations in the lunar mantle. Earth Planet. Sci. Lett. 427, 37-46.

Jochum, K.P., Stoll, B., Herwig, K., Willbold, M., Hofmann, A.W., et al., 2006. MPI-DING reference glasses for in situ microanalysis: new reference values for element concentrations and isotope ratios. Geochem. Geophys. Geosys. 7, Q02008, doi:02010.01029/02005GC001060.

Kuchka, C.R., Herd, C.D.K., Walton, E.L., Guan, Y., Liu, Y., 2017. Martian low-temperature alteration materials in shock-melt pockets in Tissint: Constraints on their preservation in shergottite meteorites. Geochim. Cosmochim. Acta 210, 228-246.

Table S1 SIMS Standards used in this study.

Material	Standard	Reference	Values used in SIMS calibration					
			H_2O (ppm)	δD (‰)	F (ppm)	S (ppm)	Cl (ppm)	P_2O_5 (wt%)
Glass	KL2-G	[a] Chen et al., 2015a,b [b] Jochum et al., 2006	64±13 [a]					0.232±0.026 [b]
	GOR128-G		145±20 [a]		25 [b]	4.3 [b]	12 [b]	0.025±0.005 [b]
	GOR132-G		130±14 [a]		22 [b]	1.8 [b]	6.2 [b]	0.036±0.012 [b]
	StHs6/80-G		120±20 [a]	-95±2 [b]	320 [b]	2.7 [b]	231±50 [b]	0.164±0.018 [b]
	MORB-1	Chen et al., 2015c	232±36			505		0.212
	ALV1645	Newcombe et al., 2014	1030				30	0.08
	WOK16-2	Newman et al., 2000	6400					
olivine	GRR1017	Bell et al., 2003; Mosenfelder et al., 2006, 2011	<1		0	0	0	
	GRR1695-2		16±5					
	GRR1784e		54±6					
orthopyroxene	San Carlos Opx	Aubaud et al., 2007	38					
	Indian Opx		141					
apatite	Ap4	McCubbin et al., 2012	5500		23900		4100	
	Ap5		3700		24500		9500	
	Ap18		2000		32800		1300	
	Ap20		300		36500		0	

[a] H_2O concentrations of these MPI-Ding glass standards (Jochum et al., 2006) were reanalyzed using FTIR (see Table S2). Note that the H_2O concentrations in KL2-G, GOR128-G, GOR132-G and StHs6/80-G are roughly half of those listed in Jochum et al. (2006).

[b] For other volatiles, the recommended values by Jochum et al. (2006) are used. MORB-1 is a piece of dehydrated JDF (Juan de Fuca Ridge) glass (Zhang and Stolper, 1991).

References for the standards

1. Aubaud, C., Withers, A.C., Hirschmann, M.H., Guan, Y., Leshin, L.A., Mackwell, S.J., Bell, D.R., 2007. Intercalibration of FTIR and SIMS for hydrogen measurements in glasses and nominally anhydrous minerals. Am. Mineral. 92, 811-828.

2. Bell, D.R., Rossman, G.R., Maldener, J., Endisch, D., Rauch, F., 2003. Hydroxide in olivine: A quantitative determination of the absolute amount and calibration of the IR spectrum. J. Geophys. Res. 108, 2105, doi:10.1029/2001JB000679.
3. Chen, Y., Liu, Y., Guan, Y., Eiler, J.M., Ma, C., Rossman, G.R., Taylor, L.A., 2015a. Evidence in Tissint for recent subsurface water on Mars. Earth Planet. Sci. Lett. 425, 55-63.
4. Chen, Y., Liu, Y., Guan, Y., Eiler, J.M., Ma, C., Rossman, G.R., 2015b. Surface and magmatic water signatures in EETA 79001 impact melts. 46th Lunar and Planetary Science Conference, #2291.
5. Chen, Y., Zhang, Y., Liu, Y., Guan, Y., Eiler, J., Stolper, E.M., 2015c. Water, fluorine, and sulfur concentrations in the lunar mantle. Earth Planet. Sci. Lett. 427, 37-46.
6. Jochum, K.P., Stoll, B., Herwig, K., Willbold, M., Hofmann, A.W., et al., 2006. MPI-DING reference glasses for in situ microanalysis: new reference values for element concentrations and isotope ratios. Geochem. Geophys. Geosys. 7, Q02008, doi:02010.01029/02005GC001060.
7. McCubbin, F.M., Hauri, E.H., Elardo, S.M., Vander Kaaden, K.E., Wang, J., Shearer, C.K.Jr., 2012. Hydrous melting of the martian mantle produced both depleted and enriched shergottites. Geology 40, 683-686, doi:10.1130/G33242.
8. Mosenfelder, J.L., Sharp, T.G., Asimow, P.D., Rossman, G.R., 2006. Hydrogen incorporation in natural mantle olivines. In S.D. Jacobsen and S. van der Lee, Eds., Earth's Deep Water Cycle p. 45-56. American Geophysical Union, Washington, D.C.
9. Mosenfelder, J.L., Le Voyer, M., Rossman, G.R., Guan, Y., Bell, D.R., Asimow, P.D., Eiler, J.M., 2011. Analysis of hydrogen in olivine by SIMS: Evaluation of standards and protocol. Am. Mineral. 96, 1725-1741.
10. Newcombe, M.E., Fabbrizio, A., Zhang, Y., Ma, C., Le Voyer, M., Guan, Y., Eiler, J.M., Saal, A.E., Stolper, E.M., 2014. Chemical zonation in olivine-hosted melt inclusions. Contrib. Mineral. Petrol. 168, 1030.
11. Newman, S., Stolper, E., Stern, R., 2000. H2O and CO2 in magmas from the Mariana arc and back arc systems. Geochemistry, Geophysics, Geosystems 1, doi:10.1029/1999GC000027.
12. Zhang, Y., Stolper, E.M., 1991. Water diffusion in basaltic melts. Nature 351, 306-309.

Table S2. FTIR measurements of MPI-DING glass standards

Standards	N [a]	$\bar{A}_{\sim 3550\ cm^{-1}}$ [b] 1/mm	2σ [b]	ε [c] L/mole/cm	ρ [d] g/cm^3	H_2O wt%	2σ wt%	Jochum et al., 2006 H_2O wt%
ATHO-G (rhyolite)	3	0.3491	0.0069	80	2.4051	0.0327	0.0006	0.0140
StHs6/80-G (andesite)	3	0.1069	0.0180	68	2.5519	0.0120	0.0020	0.0250
GOR128-G (basaltic)	7	0.1462	0.0179	63	2.8876	0.0145	0.0020	0.0260
GOR132-G (basaltic)	7	0.1319	0.0145	63	2.9059	0.0130	0.0014	0.0260
KL2-G (basaltic)	7	0.0634	0.0130	63	2.8438	0.0064	0.0013	0.0150
ML3B-G (basaltic)	3	0.0972	0.0164	63	2.8277	0.0098	0.0017	0.0150
T1-G (quartz diorite)	3	0.0807	0.0025	63	2.6296	0.0088	0.0003	0.0260

a Number of analysis.

b $\bar{A}$ is the average absorbance of the 3550 cm^{-1} band normalized to the sample thickness. 2σ is 2 sigma standard deviation around the average value.

c Molar absorption coefficients: basaltic and dacitic glass from Yamashita et al. (1997) and rhyolitic glass from Leschik et al. (2004).

d Density is calculated based on molar volumes of oxide components (Lange, 1994; Ochs and Lange, 1999) and reported oxide compositions (Jochum et al., 2006).

Lange, R.A., 1994. The effect of H2O, CO2 and F on the density and viscosity of silicate melts. Reviews in Mineralogy and Geochemistry 30, 331-369.

Ochs, F.A., Lange, R.A., 1999. The density of hydrous magmatic liquids. Science 283, 1314-1317.

Leschik, M., Heide, G., Frischat, G.H., Behrens, H., Wiedenbeck, M., Wagner, N., Heide, K., Geißler, H., Reinholz, U., 2004. Determination of H2O and D2O contents in rhyolitic glasses. Physics and Chemistry of Glasses 45, 238-251.

Yamashita, S.K., Toshihiro , Kusakabe, M., 1997. Infrared spectroscopy of hydrous glasses of arc magma compositions. Geochemical Journal 31, 169-174.

Table S3. Concentrations of H (in ppm H_2O) and major element, and hydrogen isotope compositions of olivine and pyroxene in EETA 79001.

Sample #	phase	SIMS [a]				EPMA (wt%) [b]								
		^{12}C /^{18}O ($x10^{-4}$)	H_2O (ppm)	δD (‰)	2σ error (‰)	SiO_2	TiO_2	Al_2O_3	FeO	MnO	MgO	CaO	Na_2O	Total
d.l. (wt%) [b]						0.05	0.04	0.05	0.05	0.04	0.03	0.01	0.04	
524-6	Olivine, enclosed in an impact melt		*4*	-55	60	36.9	bd	bd	32.4	0.55	31.2	0.28	bd	101.4
715-2-1	Olivine	5.77	7.0	-146	83	37.3	bd	bd	29.6	0.54	31.7	0.29	bd	99.4
524-8	Pyroxene, enclosed in an impact melt		41	2837	245	54.5	bd	0.71	17.9	0.61	21.4	5.59	bd	100.7
715-1-4	Pyroxene next to an impact melt		11	2134	226	53.4	0.20	1.06	18.3	0.70	21.0	5.37	bd	100.0
715-1-9	Pyroxene next to an impact melt		10	1729	259	51.5	0.53	0.67	24.7	0.66	16.5	5.35	bd	99.8

a: blank cell: not determined. bd: below the detection limit. The SIMS background for H_2O is 5 ppm (already subtracted) for samples (715) in indium, and ~10 ppm for the epoxy mounted section (524) and the $^{12}C^-/^{18}O^-$ value is the original SIMS count ratio.

b: d.l.: The EPMA detection limits. The analytical uncertainties (2σ) are 0.3 wt% for SiO_2, 0.2 wt% for FeO, 0.1 wt% for Al_2O_3, MgO, CaO, and Na_2O, 0.05 wt% for TiO_2 and MnO.

Table S4. Concentrations of volatiles and major element, and hydrogen isotope compositions of feldspathic glass and maskelynite in EETA 79001.

Sample #	SIMS [a]								EPMA (wt%) [b]							
	$^{12}C^-/^{18}O^-$ ($x10^{-4}$)	H_2O (ppm)	F (ppm)	S (ppm)	Cl (ppm)	P_2O_5 (wt%)	δD (‰)	2σ error (‰)	SiO_2	Al_2O_3	FeO	MgO	CaO	Na_2O	K_2O	Total
d.l. (wt%) [b]									0.05	0.05	0.05	0.03	0.01	0.03	0.01	
524-4 [c]	0.79	28	bd	bd	bd		2476	335	54.1	28.9	0.77	0.15	12.2	4.52	0.12	100.7
524-5 [c]	0.94	34	bd	bd	bd		2849	283	53.8	28.2	0.87	0.11	11.9	4.83	0.16	99.9
524-7 [d]	0.98	56	bd	bd	bd		2031	196	54.8	28.3	0.74	bd	11.0	5.14	0.24	100.2
524-11 [d]	0.73	25	bd	bd	bd		1604	311	55.4	28.0	0.57	0.07	10.8	5.42	0.24	100.5
524-11 repeat							2195	226	55.4	28.0	0.57	0.07	10.8	5.42	0.24	100.5
524-12 [e]		4					-91	82								
715-1-23 [c]	0.88	98	0.64	3.1	bd	0.025	3797	80	52.8	28.7	0.72	0.10	12.2	4.42	0.17	99.1
715-1-24 [c]	*0.89*	6	bd	bd	bd	0.027	2923	340	53.9	28.5	0.64	0.10	12.1	4.72	0.18	100.1
715-2-13 [c]	0.77	bd	bd	bd	bd	0.017			53.3	28.4	0.54	0.07	12.0	4.81	0.11	99.3
715-2-14 [c]	0.82	70	0.49	bd	bd	0.025	3938	88	53.4	28.5	0.78	0.12	12.5	3.74	0.18	99.2
717-11 [c]	0.67	bd	bd	bd	bd	0.026			53.3	28.9	0.64	0.14	12.5	4.47	0.16	100.1

a: blank cells: not determined. bd: below detection limit. The $^{12}C/^{18}O$ values are the original SIMS count ratios. The SIMS instrument backgrounds are 5 ppm for H_2O, 0.3 ppm for F, and 0.1 ppm for S and Cl, which have been subtracted from the data.

b: d.l.: The EPMA detection limits. The analytical uncertainties (2σ) are 0.3 wt% for SiO_2, 0.2 wt% for FeO, 0.1 wt% for Al_2O_3, MgO, CaO, and Na_2O, and 0.01 wt% for K_2O.

c: feldspathic glass enclosed in impact melt.

d: maskelynite ~200 μm away from impact melt pocket (524-7) or vein (524-11).

e: maskelynite far away from impact melts. Because the grain is water poor, the measured D/H may have a significant contribution of the background H. Alternatively, 715-1-24 contains a low amount of water, which could be easily affected by high D/H impact melts nearby.

Table S5. Concentrations of volatiles and major element, and hydrogen isotope compositions in the center of merrillite grains in EETA 79001.

Sample #	Close to or far away from impact melts	SIMS [a]						EPMA (wt%) [b]						
		$^{12}C/^{18}O$ ($x10^{-4}$)	H_2O (ppm)	F (ppm)	Cl (ppm)	δD (‰)	2σ error (‰)	SiO_2	FeO	MgO	CaO	Na_2O	P_2O_5	Total
d.l. (wt%) [b]								0.05	0.05	0.03	0.01	0.04	0.05	
524-Mer-40	Close to	20.6	211	bd	15	1682	187	bd	1.66	3.10	47.5	1.36	46.1	99.7
524-Mer-40 repeat						1926	148	bd	1.66	3.10	47.5	1.36	46.1	99.7
524-Mer-44	Close to	21.7	242	bd	19	3884	130	bd	2.07	2.93	47.0	1.21	45.3	98.6
524-Mer-46	Far away	18.8	223	bd	18	3282	182	0.07	2.09	2.98	47.5	1.30	45.8	99.7
715-1-Mer-4	Close to	9.52	133	bd	bd	1645	102	0.13	2.18	2.95	47.4	1.26	45.1	99.1
715-2-Mer-20	Close to	1.22	39	bd	bd	1751	129	0.08	2.17	2.83	47.2	1.30	45.8	99.4
717-Mer-37	Close to	5.50	115	bd	bd	2040	125	bd	2.23	2.97	47.3	1.22	45.4	99.2
717-Mer-37	Close to					2207	423	bd	2.23	2.97	47.3	1.22	45.4	99.2
717-Mer-37	Close to					1988	138	bd	2.23	2.97	47.3	1.22	45.4	99.2

a: blank cell: not determined. bd: below detection limit. The $^{12}C/^{18}O$ value is the original SIMS count ratio. The SIMS instrument backgrounds are 4 ppm for H_2O, 1 ppm for F, and 15 ppm for Cl. S was also analyzed but is below detection limit (0.1 ppm), which have been subtracted from the data. The EPMA detection limit for SiO_2 is 0.05 wt%.

b: d.l.: the EPMA detection limits. F, Cl, Y, and Ce were also analyzed using EPMA, but are below the detection limits (0.01 wt% for Cl, 0.05 wt% for F and Y, and 0.06 wt% for Ce). The analytical uncertainties (2σ) are 0.6 wt% for P_2O_5, 0.2 wt% for CaO, 0.1 wt% for FeO, MgO, and Na_2O, and 0.03 wt% for SiO_2.

68 Table S6. Concentrations of volatiles and major element, and hydrogen isotope compositions of impact melt in EETA 79001.

Sample #	SIMS [a]								EPMA (wt%) [b]										
	$^{12}C^-/^{18}O^-$ (10^{-4})	H_2O (ppm)	F	S	Cl	P_2O_5 (wt%)	δD (‰)	2σ error (‰)	SiO_2	TiO_2	Al_2O_3	FeO	MnO	MgO	CaO	Na_2O	K_2O	P_2O_5	Total
d.l. (wt%) [b]									0.05	0.04	0.05	0.05	0.04	0.03	0.01	0.04	0.01	0.05	
524-1	4.62	121	4.3	731	13		3955	214	51.7	0.51	7.53	16.1	0.44	13.9	8.16	1.09	bd	0.25	99.7
524-2	8.84	271	12	2639	35		4478	233	52.4	0.54	8.01	15.4	0.46	13.0	8.31	1.20	0.04	0.27	99.7
524-2							4323	250											
524-3		90					3707	236	52.8	0.23	1.00	13.5	0.52	18.1	14.1	0.12			100.4
524-9 [c]	2.53	302	13	1770	50		4133	148	51.0	0.93	8.20	16.1	0.44	12.9	8.21	1.37	0.05	bd	99.2
715-1-10	13.5	127	10	2605	31	0.356	3786	65	49.1	0.55	6.47	18.2	0.50	15.9	7.34	0.67	bd	0.55	99.2
715-1-10							3922	399	49.1	0.55	6.47	18.2	0.50	15.9	7.34	0.67	bd	0.55	99.2
715-1-10							3947	361	49.1	0.55	6.47	18.2	0.50	15.9	7.34	0.67	bd	0.55	99.2
715-1-11	4.58	167	10	707	19	0.114			50.8	0.44	8.79	15.9	0.42	13.2	7.88	1.25	0.03	0.42	99.1
715-1-12	9.52	195	13	2079	37	0.583			49.9	0.47	6.10	17.7	0.49	15.9	7.32	0.97	bd	0.52	99.4
715-1-13	9.67	169	10	2184	32	0.371			49.5	0.50	6.20	17.6	0.46	16.0	7.32	1.03	bd	0.40	99.0
715-1-14	9.67	209	10	2176	34	0.405	3643	49	49.4	0.53	6.13	18.0	0.50	16.0	7.32	0.54	0.04	0.50	98.9
715-1-15	10.2	174	10	1762	28	0.310			50.6	0.52	6.16	18.1	0.49	16.1	7.65	0.49	bd	0.40	100.4
715-1-16		176	12	2253	31	0.394			49.9	0.56	6.24	18.3	0.50	15.9	7.52	0.49	0.03	0.48	100.0
715-1-17	8.23	178	10	1998	31	0.356	4639	87	50.0	0.45	5.80	18.0	0.45	16.4	7.31	0.62	bd	0.47	99.5
715-1-18	12.4	201	10	2453	33	0.434	3368	51	49.6	0.51	6.04	18.2	0.43	16.0	7.27	0.61	bd	0.41	99.1
715-1-19	8.29	145	9.3	2257	31	0.368	3618	49	49.1	0.51	6.25	17.9	0.46	16.1	6.99	0.99	bd	0.70	99.0
715-1-20	10.5	190	10	1916	30	0.412			48.9	0.51	5.64	18.1	0.49	16.2	7.12	0.85	bd	0.39	98.3
715-1-21	8.66	194	10	1737	29	0.293			50.3	0.56	4.60	18.9	0.48	16.7	7.28	0.41	0.03	0.43	99.7
715-1-22		167	9.4	2446	30	0.354			49.6	0.53	6.49	18.1	0.39	16.1	7.33	0.63	0.03	0.45	99.6
715-2-2							4591	67	49.6	0.58	7.89	17.6	0.43	14.2	7.52	1.22	0.04	0.51	99.5
715-2-8	5.68	279	11	1741	34	0.469			50.3	0.46	6.04	17.3	0.44	16.7	6.68	1.07	0.04	0.65	99.8
715-2-9	9.53	159	10	1930	27	0.338	3922	64	49.8	0.55	5.55	18.6	0.50	16.2	7.39	0.34	0.04	0.41	99.4

715-2-10	5.75	272	11	1850	35	0.424			50.1	0.55	5.62	18.5	0.47	16.3	7.42	0.40	bd	0.49	99.8
715-2-11	6.58	377	11	1761	33	0.436	4312	47	48.8	0.48	5.51	18.0	0.44	15.9	7.30	0.95	bd	0.58	98.1
715-2-12	5.93	306	11	1905	36	0.461			49.7	0.51	5.69	18.4	0.47	15.6	7.62	0.35	bd	0.52	98.9
717-2							3858	79	48.8	0.57	6.95	18.0	0.48	14.9	7.65	0.95	bd	0.45	98.8
717-7	6.14	646	11	1855	35	0.455	3738	66	49.8	0.54	5.59	18.2	0.54	15.8	7.30	0.73	bd	0.40	98.9
717-8	6.42	526	11	1868	36	0.507			49.9	0.52	5.52	18.1	0.53	15.9	7.25	0.89	0.04	0.62	99.3
717-9	11.7	154	10	2702	36	0.412	3752	72	50.0	0.58	6.37	17.7	0.50	15.4	6.99	1.03	0.03	0.41	99.0
717-12	6.09	523	11	1831	34	0.474			48.9	0.49	5.65	17.8	0.47	15.7	7.28	1.03	bd	0.61	97.9

a: blank cell: not determined. bd: below detection limit. The ^{12}C /^{18}O value is the original SIMS count ratio. The instrument backgrounds are 8 ppm for H_2O, 1 ppm for F, 0.3 ppm for P_2O_5, and 0.1 ppm for S and Cl. All SIMS data have already subtracted backgrounds.

b: d.l.: The EPMA detection limits. The analytical uncertainties (2σ) are 0.3 wt% for SiO_2, 0.2 wt% for FeO, 0.1 wt% for Al_2O_3, MgO, CaO, Na_2O, and P_2O_5, 0.05 wt% for TiO_2 and MnO, and 0.01 wt% for K_2O.

c: Impact melt vein.

74 Table S7. Excluded SIMS data that contain cracks and holes.

Sample #	phase	SIMS [a]						EPMA (wt%) [b]									
		$^{12}C/^{18}O$ (10^{-4})	H_2O [1] (ppm)	F	Cl	δD (‰)	2σ error (‰)	SiO_2	TiO_2	Al_2O_3	FeO	MnO	MgO	CaO	Na_2O	P_2O_5	Total
717-1	olivine	53.1	4.9					36.4	bd	bd	35.2	0.66	28.6	0.27	bd	bd	101.2
715-1-1	pyroxene	123	38					54.2	0.21	1.46	14.9	0.51	17.8	11.2	0.14	bd	100.4
715-1-2	pyroxene	47.8	25					54.2	0.21	1.46	14.9	0.51	17.8	11.2	0.14	bd	100.4
715-1-3	pyroxene	9.37	21					54.2	0.21	1.46	14.9	0.51	17.8	11.2	0.14	bd	100.4
715-1-5	pyroxene	109	3.4					53.8	0.19	0.78	17.1	0.55	21.6	5.83	0.09	bd	99.9
715-1-6	pyroxene	101	73			3875	141	52.3	0.24	0.72	22.7	0.66	17.9	5.76	bd	bd	100.3
715-1-7	pyroxene	79.9	4.9					52.9	bd	0.74	17.8	0.56	22.2	5.27	bd	bd	99.5
715-1-8	pyroxene	20.9	3.9					52.9	bd	0.74	17.8	0.56	22.2	5.27	bd	bd	99.5
715-2-3	pyroxene	75.0	25					55.4	0.12	0.63	17.7	0.57	21.8	3.61	bd	bd	99.9
715-2-4	pyroxene	238	63					50.7	0.51	0.53	26.7	0.80	16.2	5.18	bd	bd	100.7
715-2-5	pyroxene	117	13					53.5	0.25	0.74	21.6	0.61	18.3	4.70	bd	bd	99.7
715-2-6	pyroxene	75.6	208					53.5	0.25	0.74	21.6	0.61	18.3	4.70	bd	bd	99.7
715-2-7	pyroxene	189	12			1543	417	50.0	0.76	0.73	25.5	0.78	15.6	6.78	bd	bd	100.2
717-4	pyroxene	365	16					52.4	0.29	1.06	22.5	0.69	17.7	5.47	bd	bd	100.2
717-5	pyroxene	53.3	20					53.6	0.21	0.88	17.9	0.57	20.7	5.79	bd	bd	99.8
717-6	pyroxene	66.1	10			2572	217	52.5	0.13	0.91	16.7	0.57	21.9	6.20	0.09	bd	98.9
524-Mer-47	Merrillite close to	956	543	bd	49			0.07			2.09		2.98	47.5	1.30	45.8	99.8
715-1-Mer-5	Merrillite in impact melt	269	47	bd	bd	2532	110	bd			1.84		2.97	47.6	1.31	45.4	99.2
715-1-Mer-17	merrillite in impact melt	3.61	76	8.1	9.5	4133	109	0.13			2.98		2.74	47.5	0.55	45.3	99.2
715-2-Mer-28	merrillite	7.66	147	bd	bd	3226	253	bd			2.14		2.99	47.5	1.28	46.1	100.0
717-Mer-38	merrillite	280000	6896	9.1	1396			bd			2.24		2.83	47.2	1.18	45.6	99.1
524-10	impact melt	1.32	61	1.2	bd	296	206	53.5	0.14	0.83	16.9	0.52	22.4	4.77	bd	bd	99.6

75 a: blank cell: not determined. bd: below detection limit. The SIMS instrument backgrounds in silicate minerals and glass are 5 ppm for H_2O, 0.3 ppm for F, and
76 0.1 ppm for S and Cl. The SIMS instrument backgrounds in merrillite are 4 ppm for H_2O, 1 ppm for F, and 15 ppm for Cl. All SIMS data have subtracted
77 backgrounds.

78 b: The EPMA detection limits in silicate minerals and glass are 0.1 wt% for Al_2O_3, Na_2O, and P_2O_5, 0.05 wt% for TiO_2, and 0.01 wt% for K_2O. The EPMA
79 detection limit for SiO_2 in merrillite is 0.05 wt%.

80

Fig. S1 Transmitted light image of EETA 79001, 524, and reflective light (right) image of the impact melt in the red box. Olivine and pyroxene locations in Table 1 are labelled. Dotted line separates the melt pocket from host rock. Scale bars are 0.5 mm.

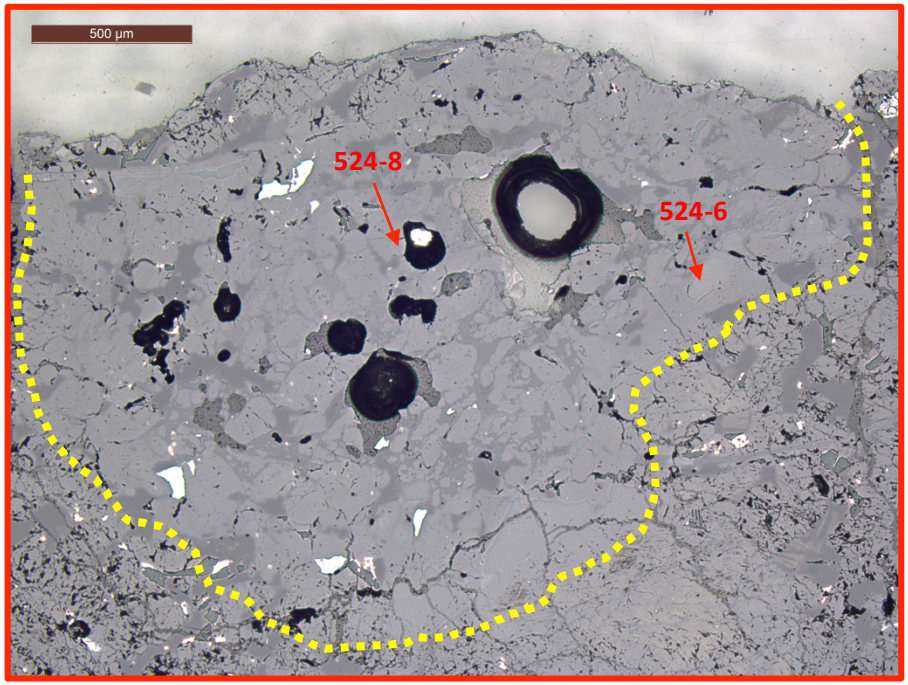

85 Fig. S2. Backscattered electron (BSE) image of EETA 79001, 715, section #1. This chip appears to be fully from impact melt pocket. Red box
86 outlines the area containing Merrillite #5 in Fig. 2. SIMS analyses of feldspar glass were labeled by arrowed lines.

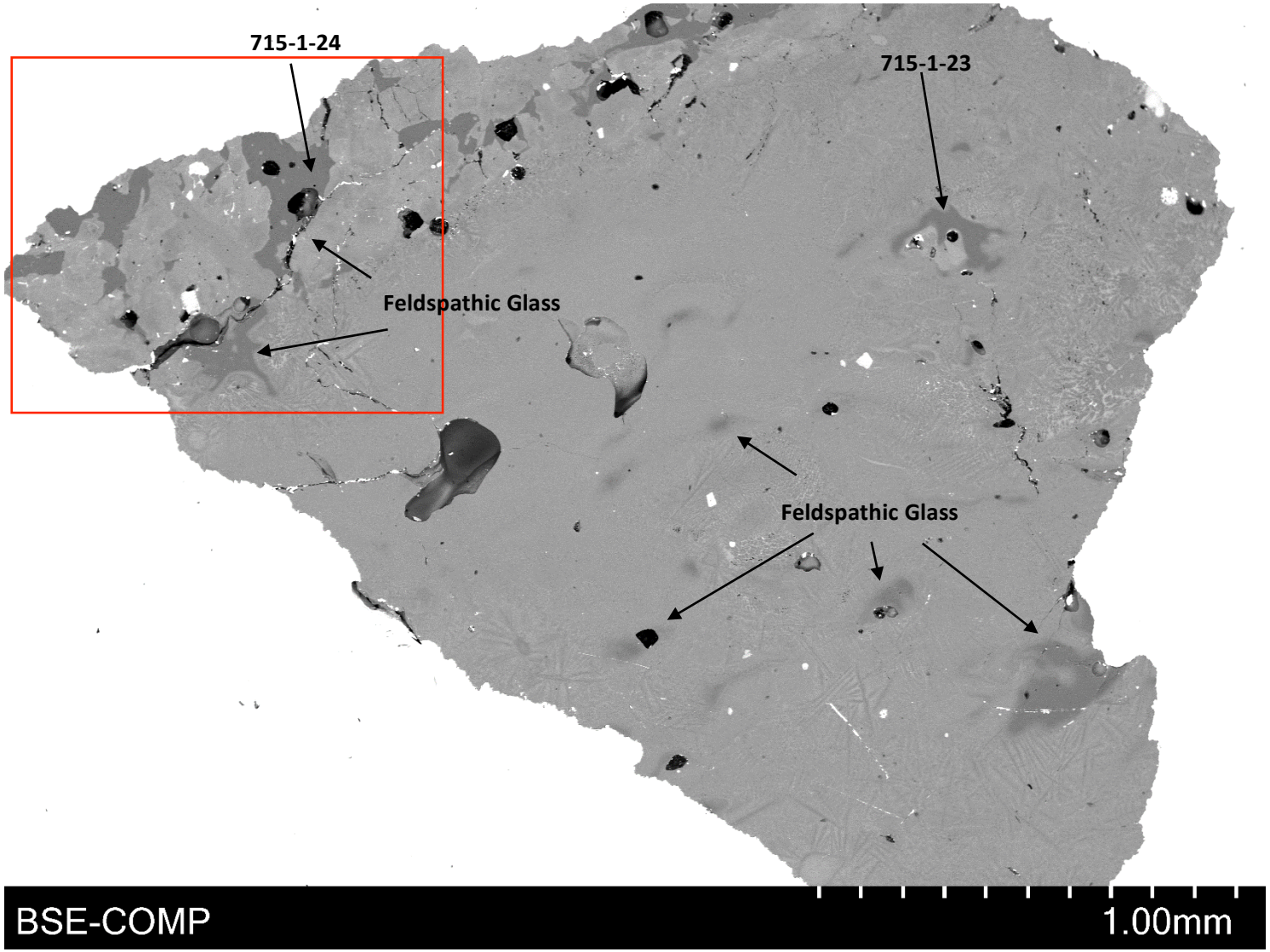

87

Fig. S3. BSE image of EETA 79001, 715, section #2. Red box marks the area (BSE image) containing Merrillite #20 in Fig. 2. Dotted line separates the melt pocket from host rock.

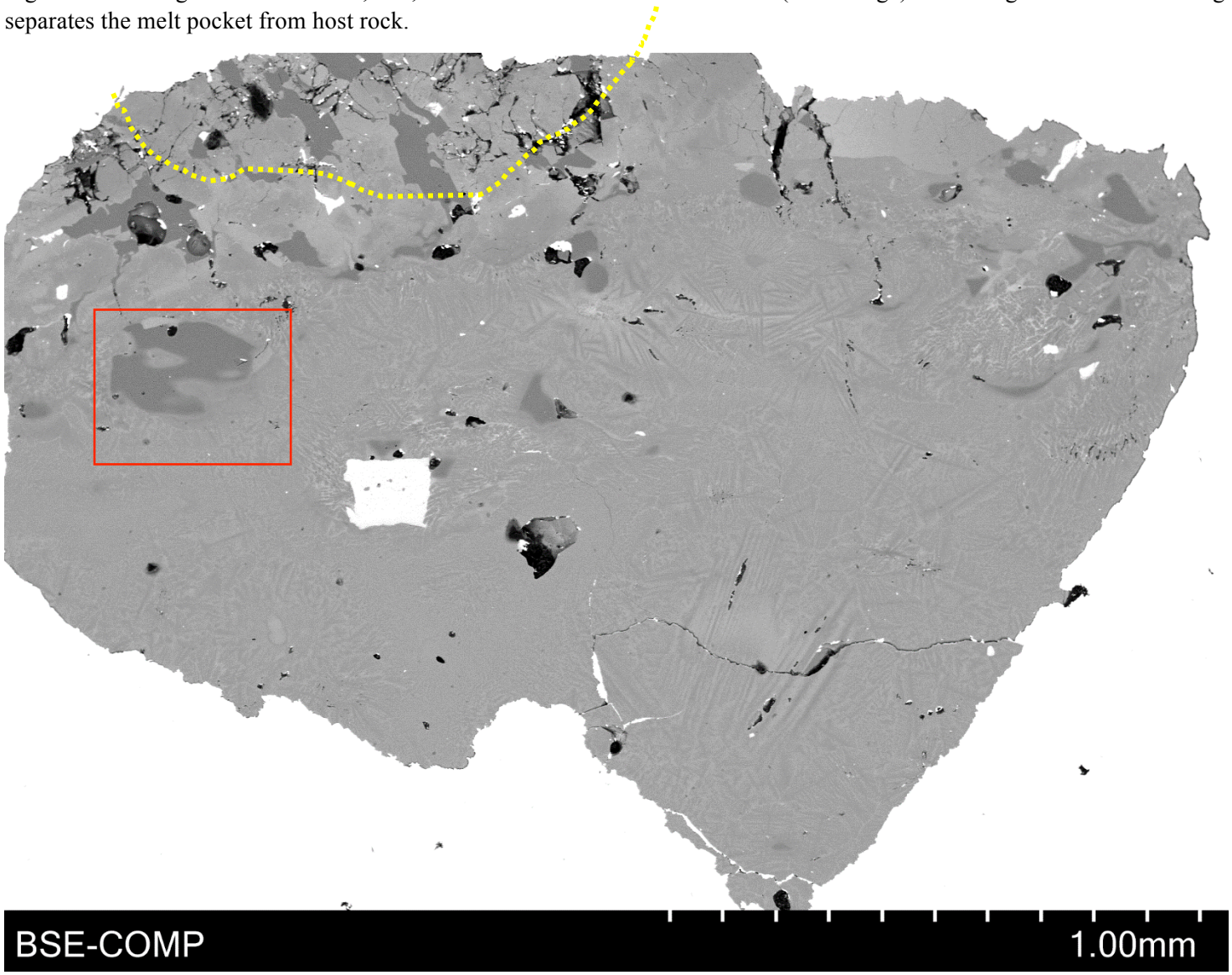

Fig. S4. Reflective light image of a chip from EETA 79001, 717. This chip appears to be fully from impact melt pocket. Dotted line marks the boundary between impact melt pocket and host rock

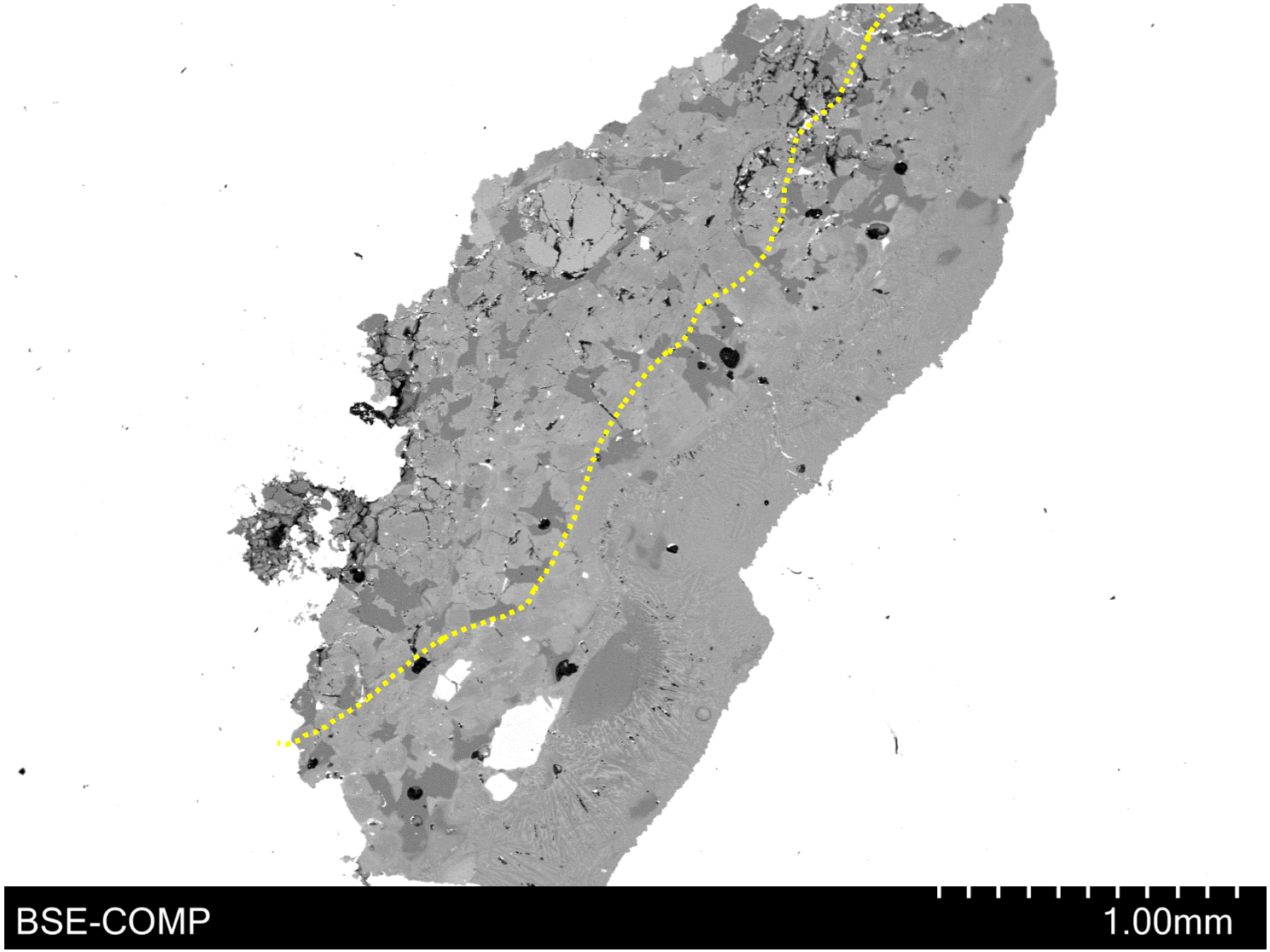

Fig. S5. BSE images of the SIMS analysis positions, ordered as in Table S3 – S6

Olivine and pyroxene in Table S3

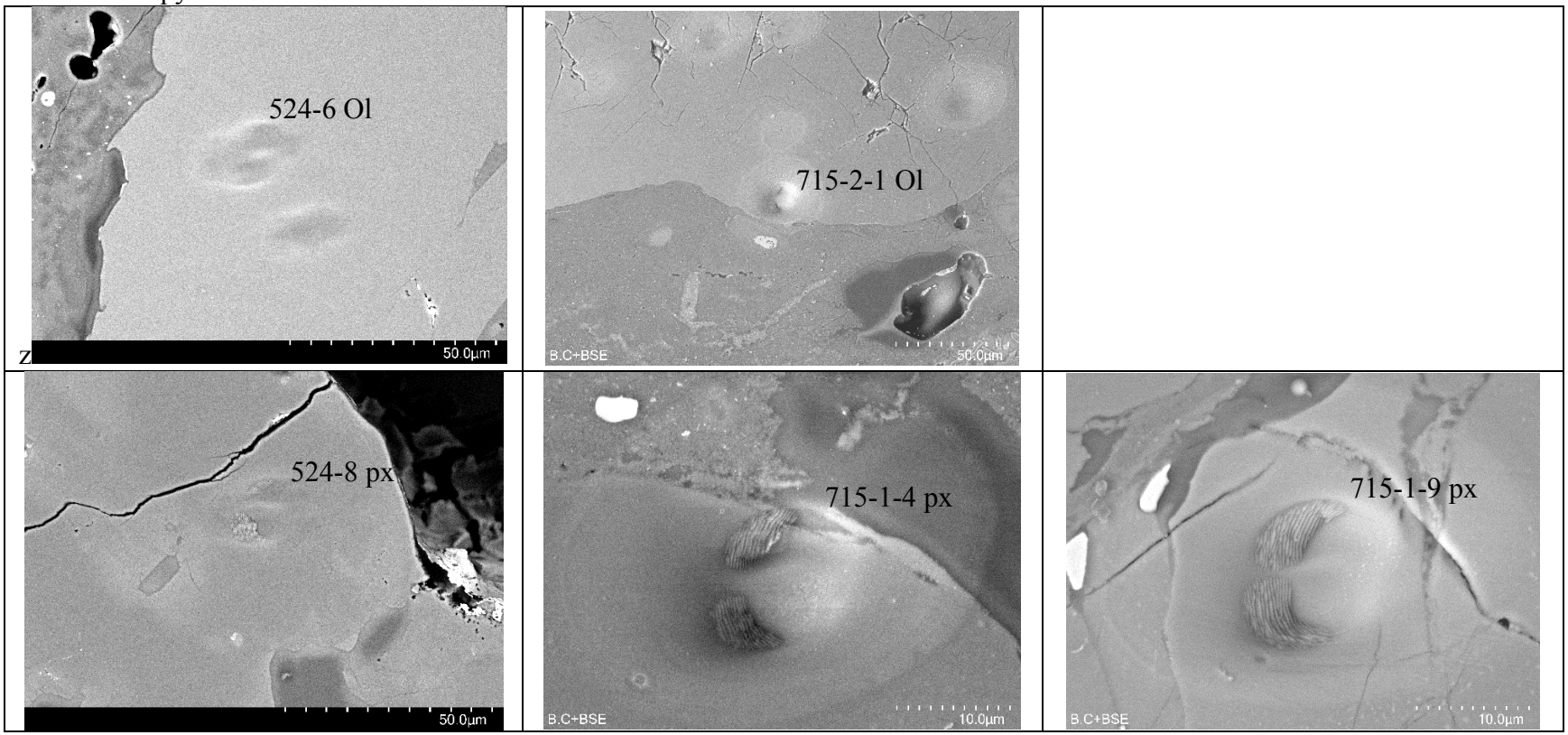

Merrillite in Table S5

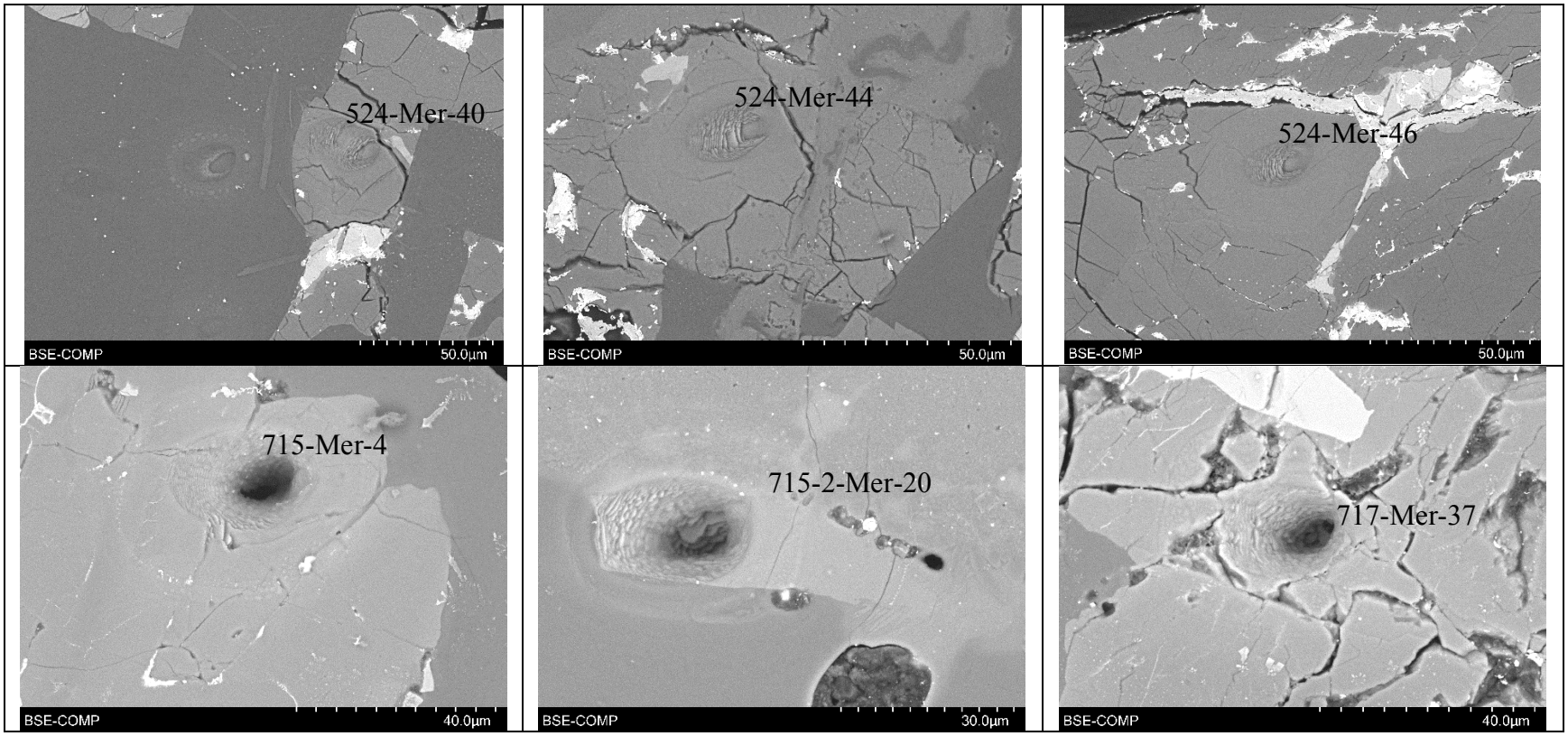

101 Maskelynite (524-7) and feldspathic glass in Table S3

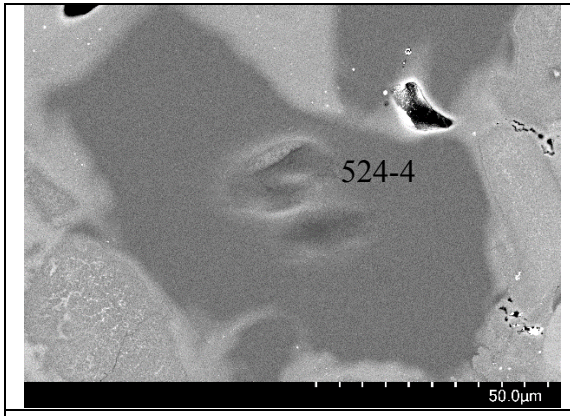	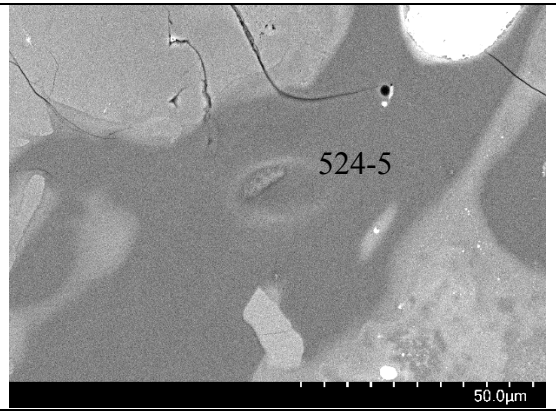	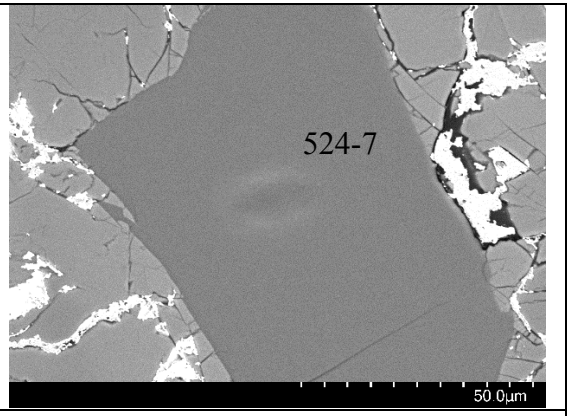
Feldspathic glass	Feldspathic glass	Maskelynite, ~200 µm from impact melt pocket
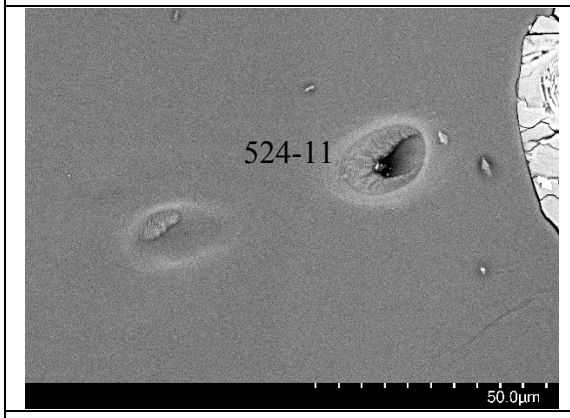	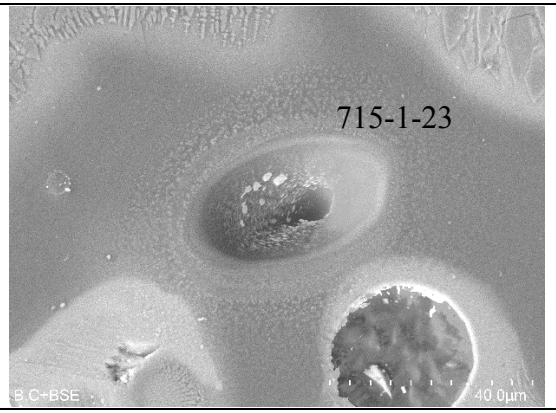	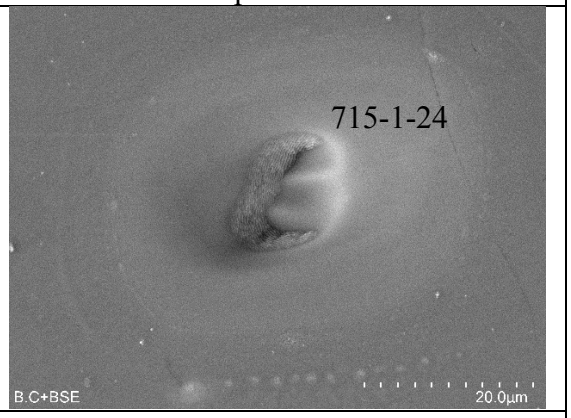
Maskelynite, ~200 µm from impact mlett vein	Feldspathic glass	Feldspathic glass

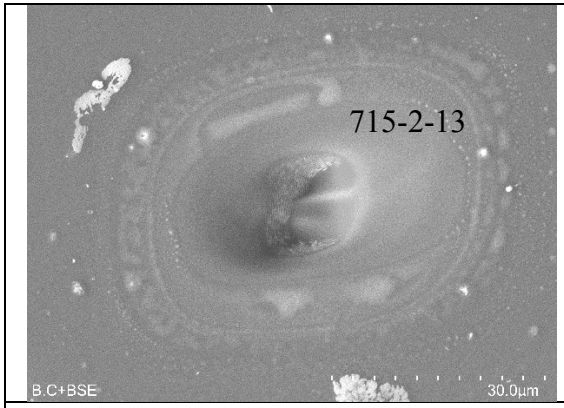	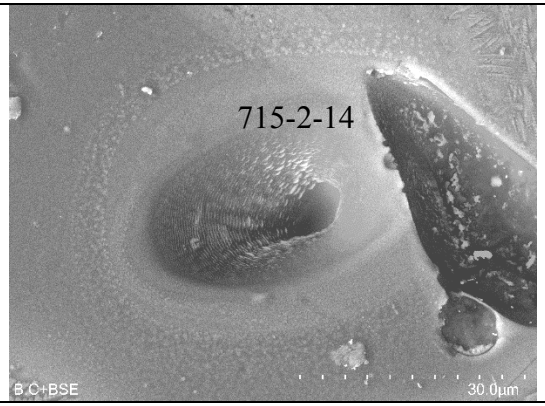	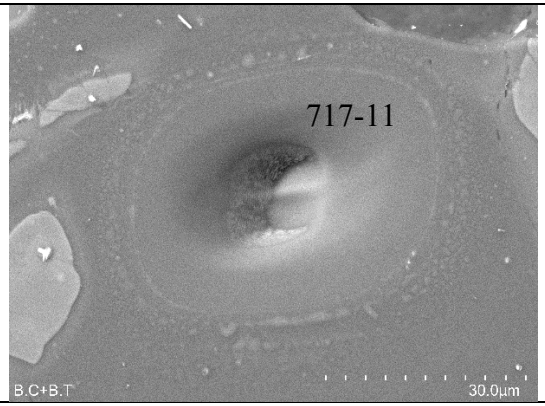
Feldspathic glass	Feldspathic glass	Feldspathic glass
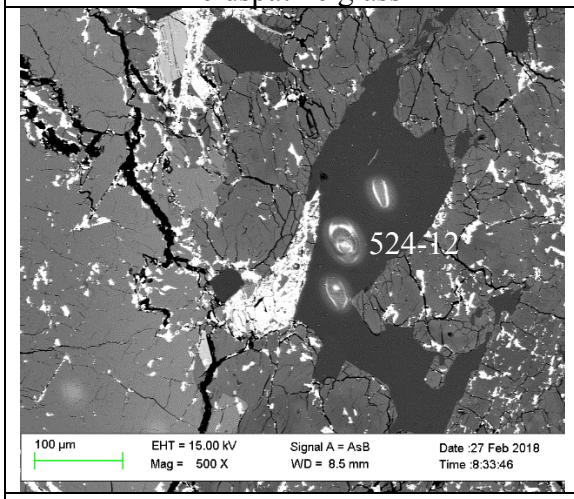		
Maskelynite		

102

103 Impact melts in Table S6.

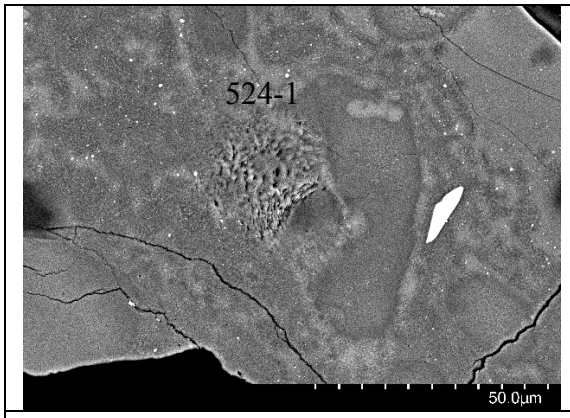

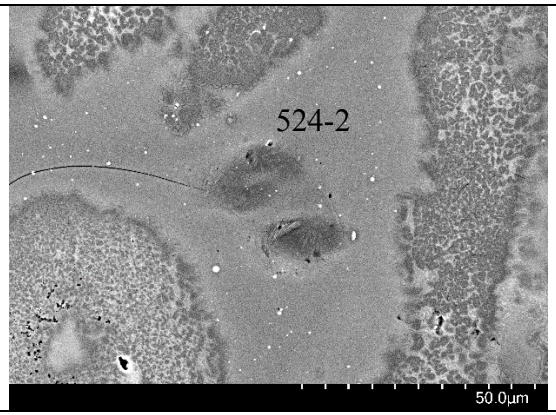

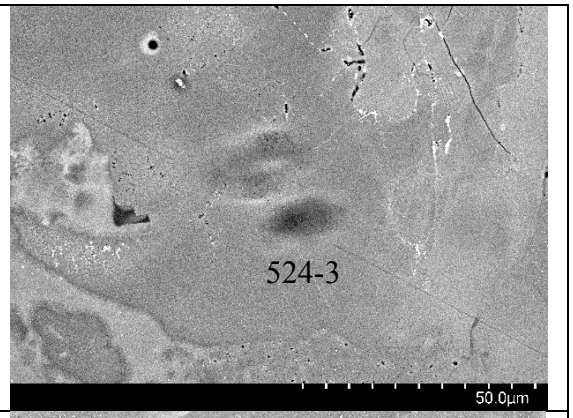

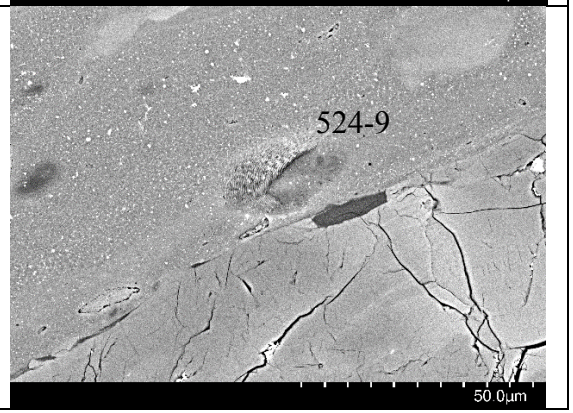

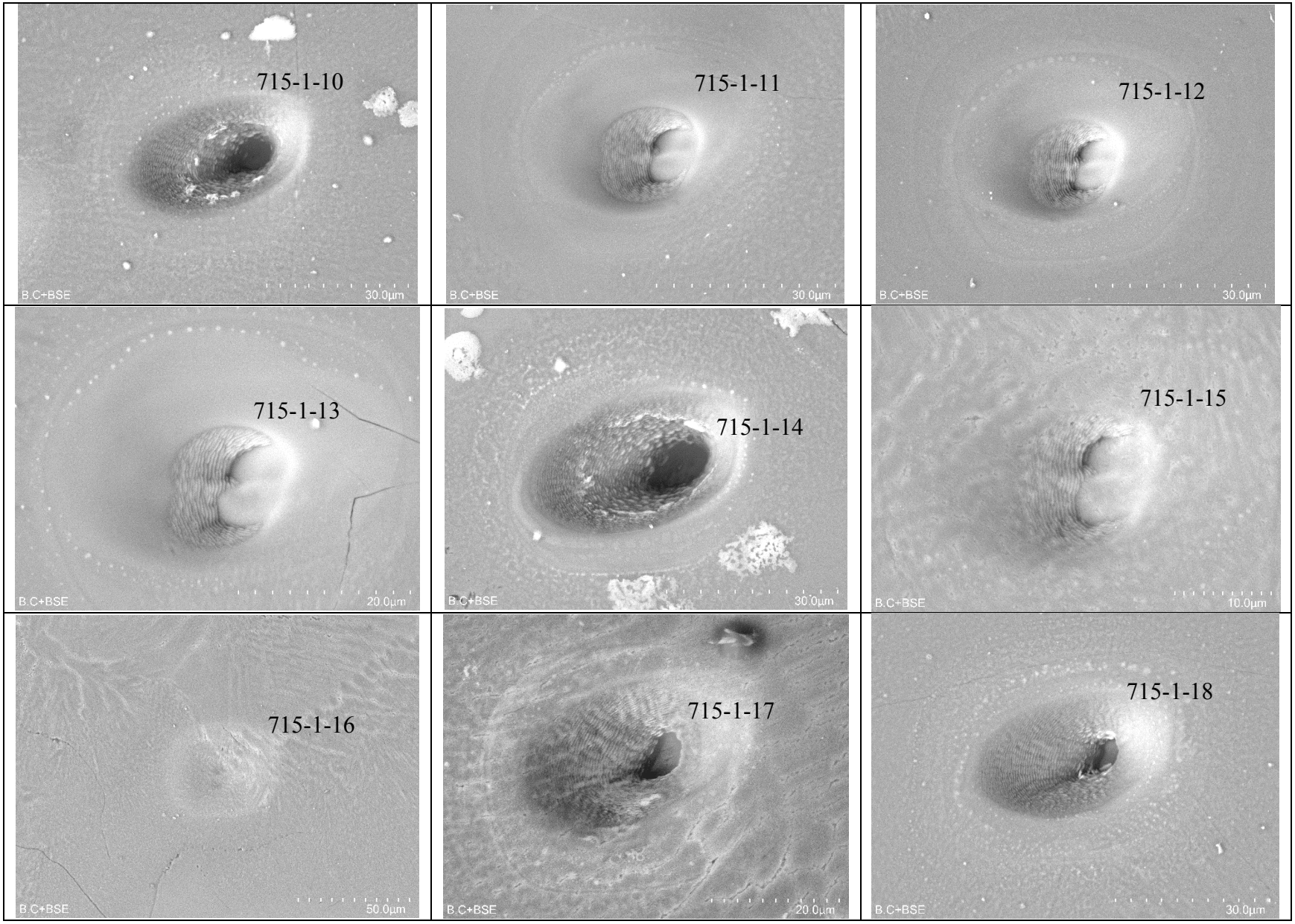
715-1-10
B.C+BSE
30.0µm
715-1-11
B.C+BSE
30.0µm
715-1-12
B.C+BSE
30.0µm
715-1-13
B.C+BSE
20.0µm
715-1-14
B.C+BSE
30.0µm
715-1-15
B.C+BSE
10.0µm
715-1-16
B.C+BSE
50.0µm
715-1-17
B.C+BSE
20.0µm
715-1-18
B.C+BSE
30.0µm

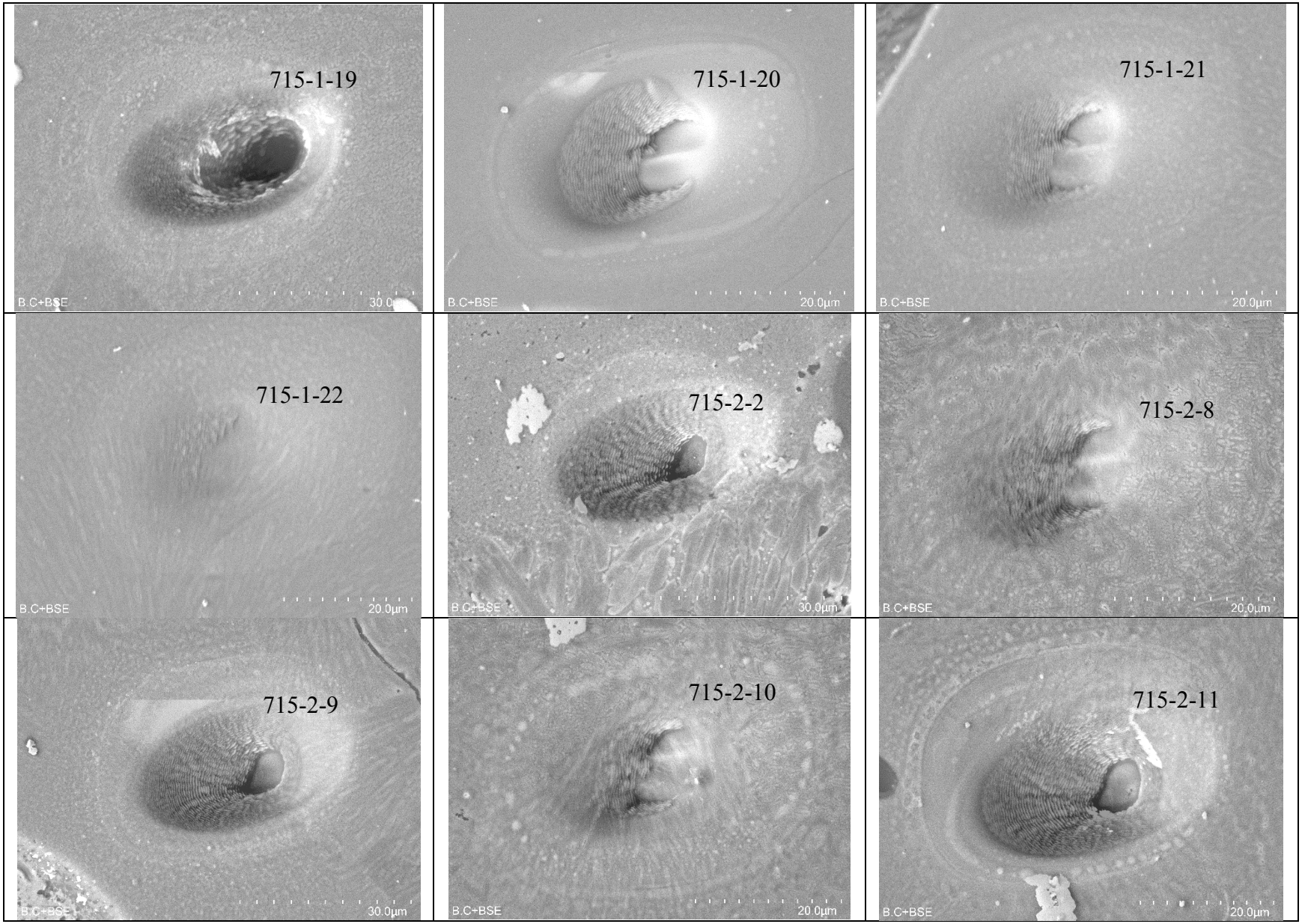
715-1-19
B.C+BSE
715-1-20
B.C+BSE 20.0µm
715-1-21
B.C+BSE 20.0µm
715-1-22
B.C+BSE 20.0µm
715-2-2
B.C+BSE 30.0µm
715-2-8
B.C+BSE 20.0µm
715-2-9
B.C+BSE 30.0µm
715-2-10
B.C+BSE 20.0µm
715-2-11
B.C+BSE 20.0µm

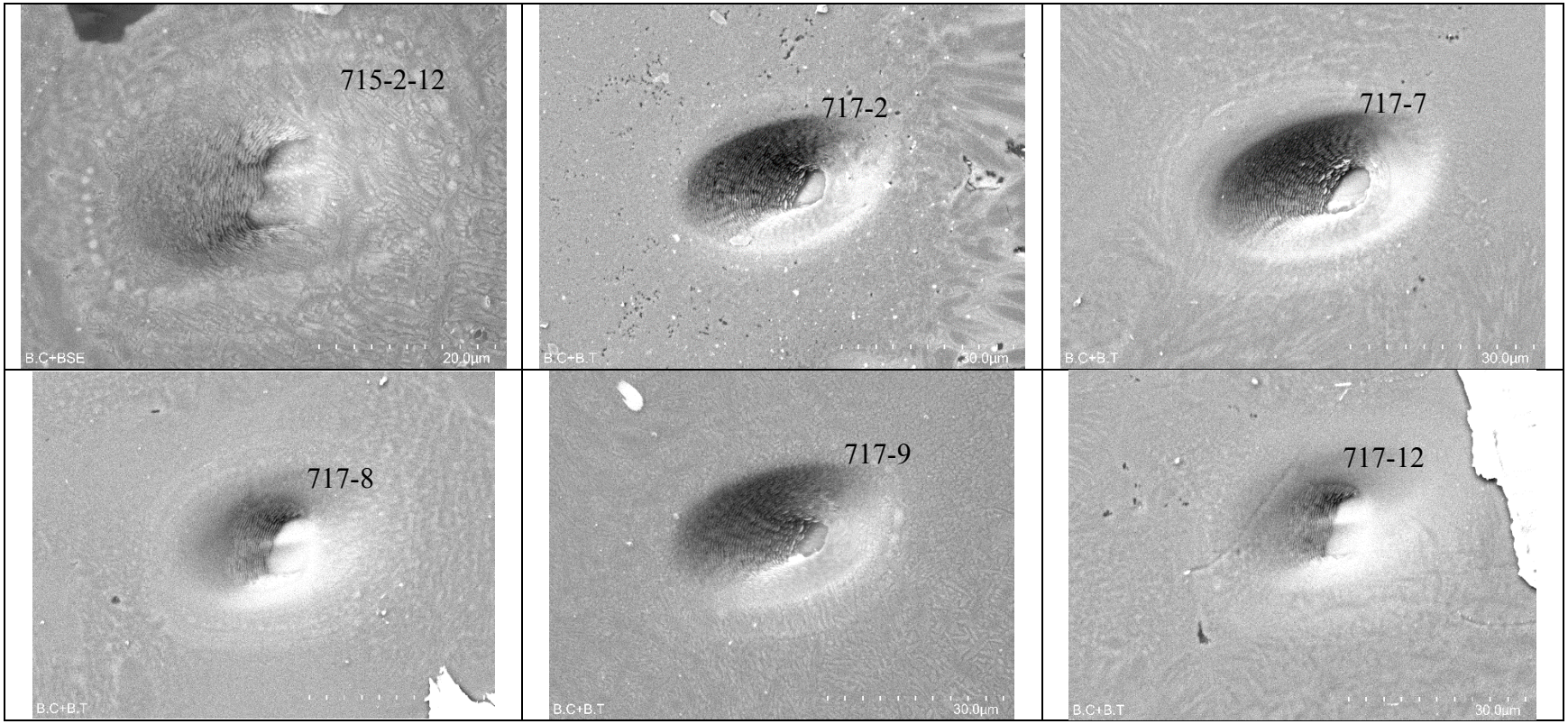
715-2-12
B.C+BSE
20.0µm
717-2
B.C+B.T
30.0µm
717-7
B.C+B.T
30.0µm
717-8
B.C+B.T
717-9
B.C+B.T
30.0µm
717-12
B.C+B.T
30.0µm

104

105 Fig. S6. BSE images of the excluded data, ordered as in Table S7.

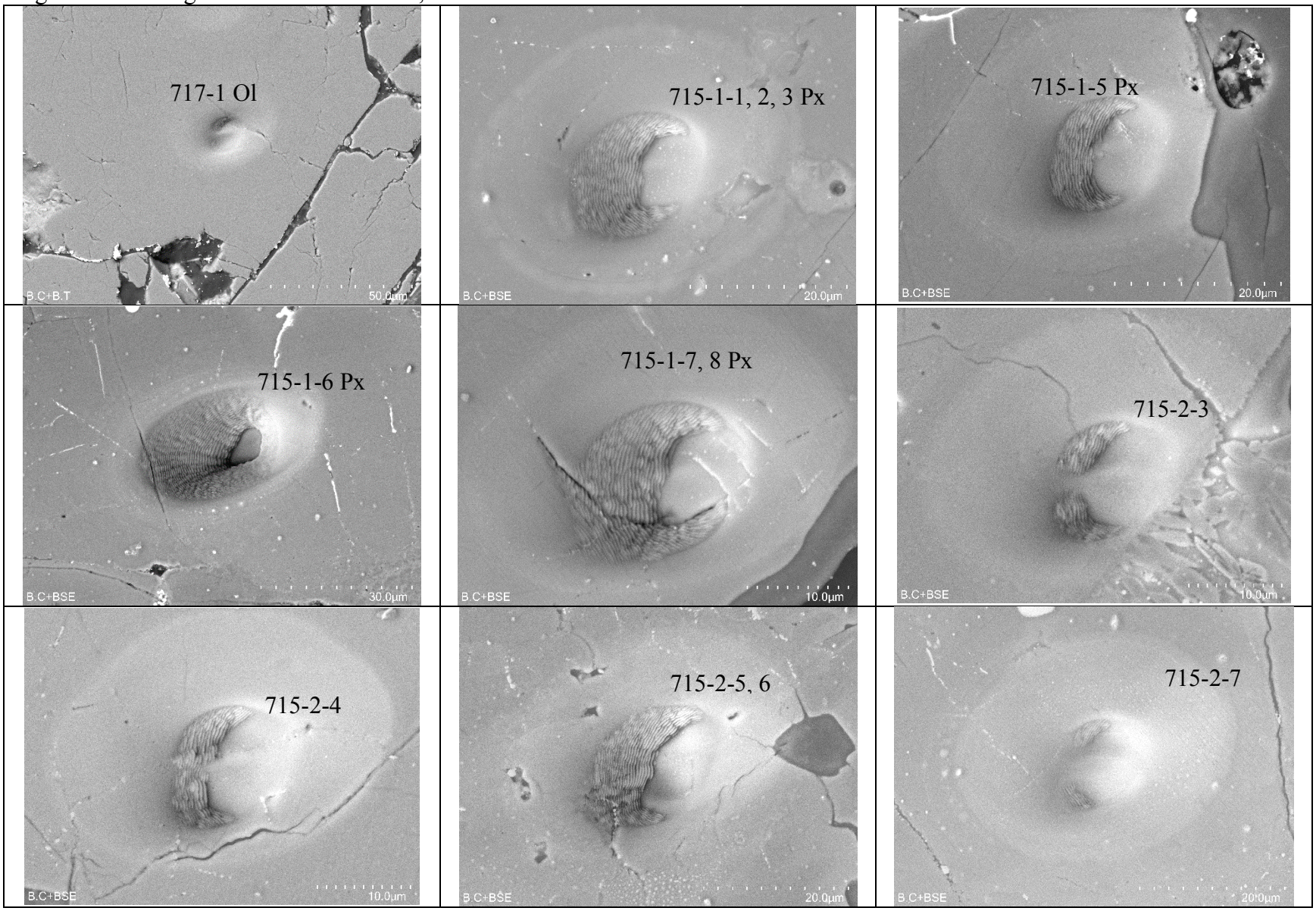

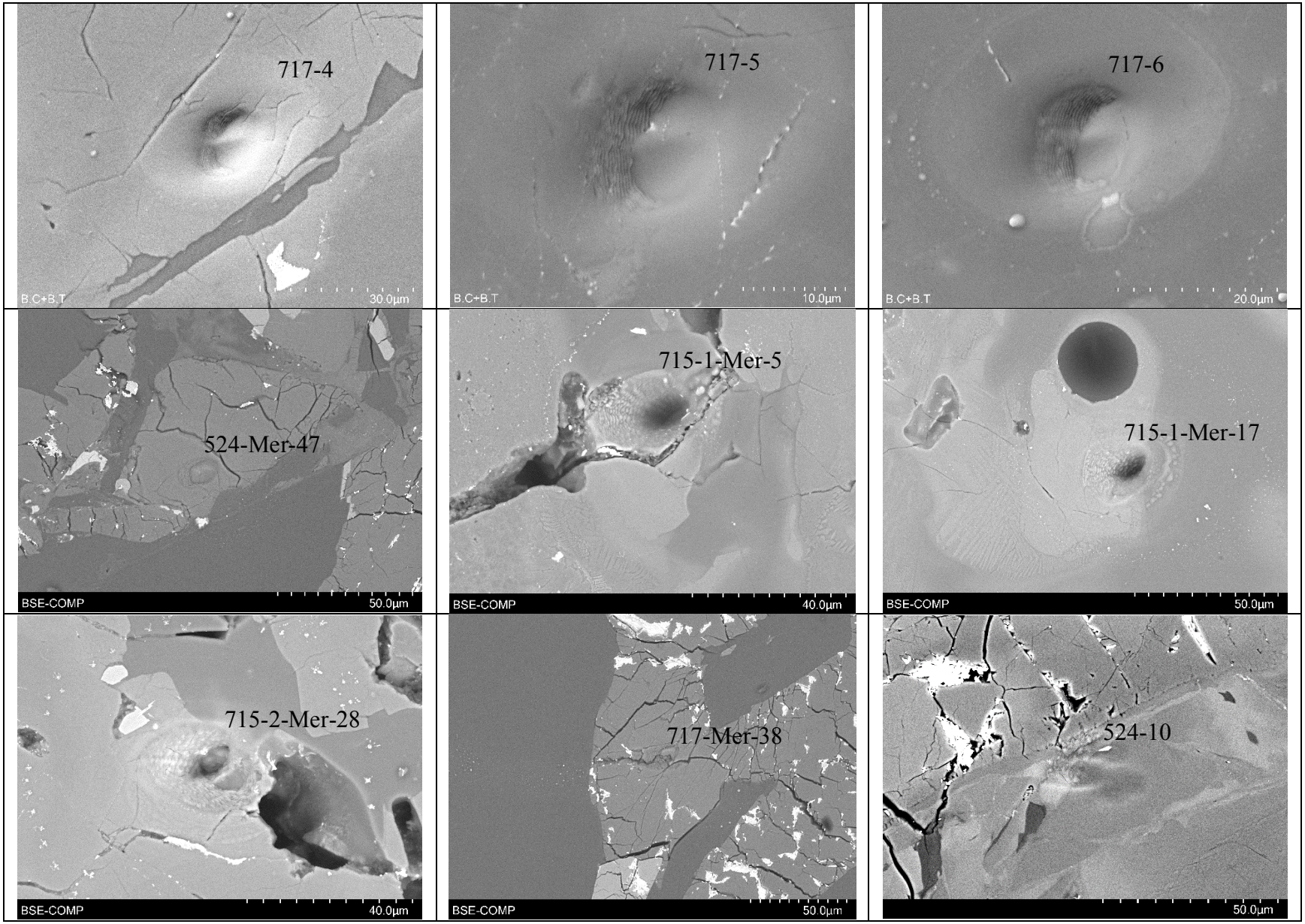
717-4
B.C+B.T
30.0µm
717-5
B.C+B.T
10.0µm
717-6
B.C+B.T
20.0µm
524-Mer-47
BSE-COMP
50.0µm
715-1-Mer-5
BSE-COMP
40.0µm
715-1-Mer-17
BSE-COMP
50.0µm
715-2-Mer-28
BSE-COMP
40.0µm
717-Mer-38
BSE-COMP
50.0µm
524-10
50.0µm

106